

Human bone marrow mesenchymal stem cell-derived extracellular vesicles inhibit shoulder stiffness via let-7a/Tgfr1 axis

Zhiwen Luo^{b,1}, Yaying Sun^{b,1}, Beijie Qi^{b,1}, Jinrong Lin^b, Yisheng Chen^b, Yuzhen Xu^c, Jiwu Chen^{a,*}

^a Department of Sports Medicine, Shanghai General Hospital, Shanghai Jiao Tong University, School of Medicine, Shanghai Jiao Tong University, Shanghai, China

^b Department of Sports Medicine, Huashan Hospital, Fudan University, Shanghai, China

^c Department of Rehabilitation, The Second Affiliated Hospital of Shandong First Medical University, Shandong Province, China

ARTICLE INFO

Keywords:

Shoulder stiffness
Adhesive capsulitis
Extracellular vesicles
Human bone marrow mesenchymal stem cell
MicroRNA
Fibrosis

ABSTRACT

Shoulder stiffness (SS) is a common shoulder disease characterized by increasing pain and limited range of motion. SS is considered to be an inflammatory and fibrotic disorder pathologically. However, there is no consensus on the most effective conservative treatment for fibrosis. Given that human Bone Marrow Mesenchymal Stem Cell-derived extracellular vesicles (BMSC-EVs) displayed promising therapeutic effects for various tissues, we investigated the therapeutic effect of BMSC-EVs on fibrosis in a mice immobilization model and two cell models. By conducting a series of experiments, we found that BMSC-EVs can significantly inhibit the fibrogenic process both *in vitro* and *in vivo*. In detail, BMSC-EVs suppressed the aberrant proliferation, high collagen production capacity, and activation of fibrotic pathways in TGF- β -stimulated fibroblasts *in vitro*. Besides, *in vivo*, BMSC-EVs reduced cell infiltration, reduced fibrotic tissue in the shoulder capsule, and improved shoulder mobility. In addition, via exosomal small RNA sequencing and qPCR analysis, let-7a-5p was verified to be the highest expressed miRNA with predicted antifibrotic capability in BMSC-EVs. The antifibrotic capacity of BMSC-EVs was significantly impaired after the knockdown of let-7a-5p. Moreover, we discovered that the mRNA of TGFBR1 (the membrane receptor of transforming growth factor β) was the target of let-7a-5p. Together, these findings elucidated the antifibrotic role of BMSC-EVs in shoulder capsular fibrosis. This study clarifies a new approach using stem cell-derived EVs therapy as an alternative to cell therapy, which may clinically benefit patients with SS in the future.

1. Background

Shoulder stiffness (SS), either primary or secondary, is a painful condition impairing glenohumeral motion [1–3]. The lifetime incidence of primary SS reported in the general population is 2–5% [4,5] and can last for several years [6,7]. Secondary SS can be subject to trauma or surgery [8]. Understanding the pathology of SS is important for developing treatment strategies.

Triggered by inflammation, SS is characterized by thickening, stiffening, and fibrosis of joint capsule [9,10]. Numerous treatments were proposed against inflammation [11–13]. For example, Sun et al. reported that steroid injection was effective against SS in inflammatory stage [14,15]. Besides, oral anti-inflammatory drugs and intra-articular

hyaluronate injection are also applied clinically [16,17]. However, once inflammation is not inhibited sufficiently and fibrogenesis is initiated, few conservative modalities can successfully inhibit this progress, and surgical interventions are unavoidable [18]. Current research of FS is still in progress to understand the etiology of primary FS and how to treat it non-invasively for FS with fibrosis [13]. Investigating the properties of SS-related fibrosis is essential in searching for novel non-invasive treatments.

Like other fibrotic disorders, SS-related fibrosis is characterized by recruitment, proliferation, and activation of fibroblasts [19]. Stimulated by local cytokines and growth factors, these cells produce much collagen into extracellular space [20], resulting in excessive accumulation of extracellular matrix (ECM) and stiffened tissue [21]. Stimulated by local

Peer review under responsibility of KeAi Communications Co., Ltd.

* Corresponding author. Shanghai General Hospital, No. 85 Wujin Road, Hongkou District, Shanghai, China.

E-mail address: jeevechen@gmail.com (J. Chen).

¹ These authors make equal contributions to this work.

<https://doi.org/10.1016/j.bioactmat.2022.01.016>

Received 24 August 2021; Received in revised form 30 December 2021; Accepted 9 January 2022

Available online 23 January 2022

2452-199X/© 2022 The Authors. Publishing services by Elsevier B.V. on behalf of KeAi Communications Co. Ltd. This is an open access article under the CC BY-NC-ND license (<http://creativecommons.org/licenses/by-nc-nd/4.0/>).

cytokines and growth factors, these cells produce much collagen into the extracellular space, resulting in excessive extracellular matrix (ECM) accumulation and stiffened tissue. Inhibiting the proliferation and collagen synthesis of fibroblasts is an important part of breaking the fibrotic cycle. Inhibiting fibroblasts' proliferation and collagen synthesis are essential for breaking the fibrotic cycle.

In recent years, much attention has been attracted to the anti-fibrotic potential of extracellular vesicles (EVs), especially those derived from mesenchymal stem cells. With a diameter of 40–150 nm, EVs contain nucleic acids, proteins, and other bioactive substances, which can be absorbed by target cells [22]. Emerging evidence highlights the significance of exosomal microRNAs (miRs) in treating many diseases [23–28]. For example, it was found that MSC-EVs with miR-125b-5p can be effective in treating ischemic acute kidney injury, while MSC-EVs were proved to cure pulmonary hypertension based on their miR cargo [29,30]. Moreover, MSC-EVs with upregulating miR-133a-3p could alleviate acute myocardial infarction [31]. Several types of MSC-EVs were reported in recent years, and in this study, we chose bone marrow mesenchymal stem cell-derived EVs (BMSC-EVs) to treat shoulder stiffness. In clinical therapy, BMSC-EVs can avoid some of the drawbacks of BMSC-transplantation therapy (graft rejection, ethical issues, and potential tumor formation, etc.) and have the advantages of high stability, easy storage, no need for cell proliferation, easy dosing, and ability of recruitment to the injury (similar to their original cells) [32]. BMSC-EVs were applied to many diseases such as heart fibrosis, skeletal muscle fibrosis [20], COVID-19, ischemic stroke, and so forth [32–34]. At present, the two most widely used EVs are BMSC-EVs (from bone marrow) and AMSC-EVs (from adipocytes), while the research of ESC-EVs (from embryonic stem cells) is still at the preliminary stage [35]. Recently, two studies have compared the therapeutic effects of BMSC-EVs and AMSC-EVs. Fazaeli et al. found that BMSC-EVs could result in better outcomes for osteoarthritis than AMSC-EVs [36]. Through miRNAs sequencing and the bioinformatic analysis, Pomatto et al. reported that BMSC-EVs could promote more robust cell viability than AMSC-EVs [37]. Therefore, even AMSC-EVs are relatively easier to obtain [38], BMSC-EV is still the first choice among all these stem cell-derived EVs for us.

Therefore, in this study, we tested whether BMSCs-derived exosomal miRNAs could inhibit shoulder capsular fibrosis in a mouse model. Therefore, we tested whether BMSCs-derived exosomal miRNAs could inhibit shoulder capsular fibrosis in a mouse model in this study. For experiments *in vitro*, capsular-derived fibroblasts (CDFs) harvested from shoulder capsule samples collected during surgery were used. The related mechanisms were also delineated.

2. Methods

This study was approved by the local ethical committee of Huashan Hospital, Fudan University (KY-2018-0390). All patients were offered informed consent for tissue collection and cell extraction, and this study was conducted following the Declaration of Helsinki. All the animal experiments were approved by the Institutional Animal Care and Use Committee (202004003S) of Huashan Hospital, Fudan University, meanwhile were conducted according to the Guide for the Care and Use of Laboratory Animals. All efforts were carried out to minimize animal suffering. We have submitted all relevant information of our experiments to the EV-TRACK knowledgebase according to EV-TRACK knowledgebase (ID: EV210463), which is the official standard for extracellular vesicle-related studies [39]. The whole experimental flow chart including treatments, timepoints, procedures, and test methods was presented in [Supplemental Fig. 1](#).

2.1. Patients inclusion and sample collection

Patients with SS of stage II were selected according to the published criteria [40]. Inclusion criteria were 1) Patients with SS and without

abnormal findings on radiography, magnetic resonance imaging, or ultrasound; 2) Resistant to conservative treatment for at least 6 months; 3) Shoulder ROM (range of motion) was limited in all directions, especially in external rotation at 0° of abduction (ER₀). Exclusion criteria were patients with shoulder stiffness after humeral head fracture with glenohumeral osteoarthritis, internal fixation, locked dislocation, shoulder surgery, or tumor, labral tear, and biceps tendon/rotator cuff tear identified during surgery. After inclusion and exclusion procedures, the shoulder capsule samples were harvested. The samples of patients with SS of stage II were named SS group, while capsule samples of patients with rotator cuff tear with full ROM during arthroscopic surgery (RCT group), were also collected.

2.2. Cell culture

Human bone marrow stem cells (hBMSCs) were purchased from ScienCell Research Laboratories. Cells were cultured in the complete mesenchymal stem cell medium (ScienCell Research Laboratories) in a humidified incubator (37 °C, 5% CO₂).

For mice fibroblasts, NIH3T3 cells were purchased from Shanghai Cell Bank and cultured in high-glucose DMEM (Thermo Fisher Scientific, USA) + 10% fetal bovine serum (FBS, Gibco, USA) + 1% penicillin/streptomycin solution (ScienCell) in a humidified incubator (5% CO₂ atmosphere, 37 °C). Before interventions, 2×10^6 cells were seeded in a 6-well plate for further experiments.

To obtain the human capsule-derived fibroblasts (CDFs), fresh capsular samples were harvested in the RCT group, and 13 patients with the SS group. Then, the CDFs were collected following the published protocol [41]. Afterward, CDFs were cultured in high-glucose DMEM medium (Thermo Fisher Scientific) + 10% FBS (Gibco) + 1% penicillin/streptomycin solution. The harvested CDFs were seen as passage zero. When reaching 80–90% confluence, CDFs were passaged, and CDFs of passage 3 were used in further experiments. Abovementioned cells were all maintained in a humidified incubator with 5% CO₂ atmosphere at 37 °C.

2.3. Cell intervention and transfection

After cell (CDFs or NIH3T3) reached 80% confluence, the growth medium was re-added serum-free medium for interventions. The concentration of transforming growth factor-β (TGF-β, Sigma, St Louis, USA) was 20 ng/ml for 24h. The final concentration of BMSC-EVs was 20ug/ml or 50ug/ml for 24h (equal to final particles from 2.25×10^9 to 6×10^9 /ml).

The cell transfection was performed with the Lipofectamine 3000 Reagent (Invitrogen) following the manufacturer's protocol. The small interfering RNAs (50 nM) against TGFBR1 and negative control (si-NC) were all obtained from Sangon Biotech. To knockdown or overexpress let-7a-5p, let-7a-5p mimics (20 nM), let-7a-5p inhibitor (50 nM), and its negative controls were purchased from Sangon Biotech and were transfected into cells for 24h. The sequences were shown in [Supplemental Table 1](#).

2.4. BMSC identification

To evaluate morphological characteristics of BMSC, cells with different confluence were pictured directly under an optical microscope. Besides, to access the differentiation ability of this kind of cell, different interventions (commercial kits for adipogenesis/osteogenesis/chondrogenesis induction, YuBo biology co., Ltd., China) were applied. In addition, Oil red O staining was used to confirm adipogenesis, Alizarin red staining was performed to verify osteogenesis, and Safranin O staining was applied to examine chondrogenesis. Moreover, the negative and positive surface markers of BMSC were identified by flow cytometry (described in the following method section).

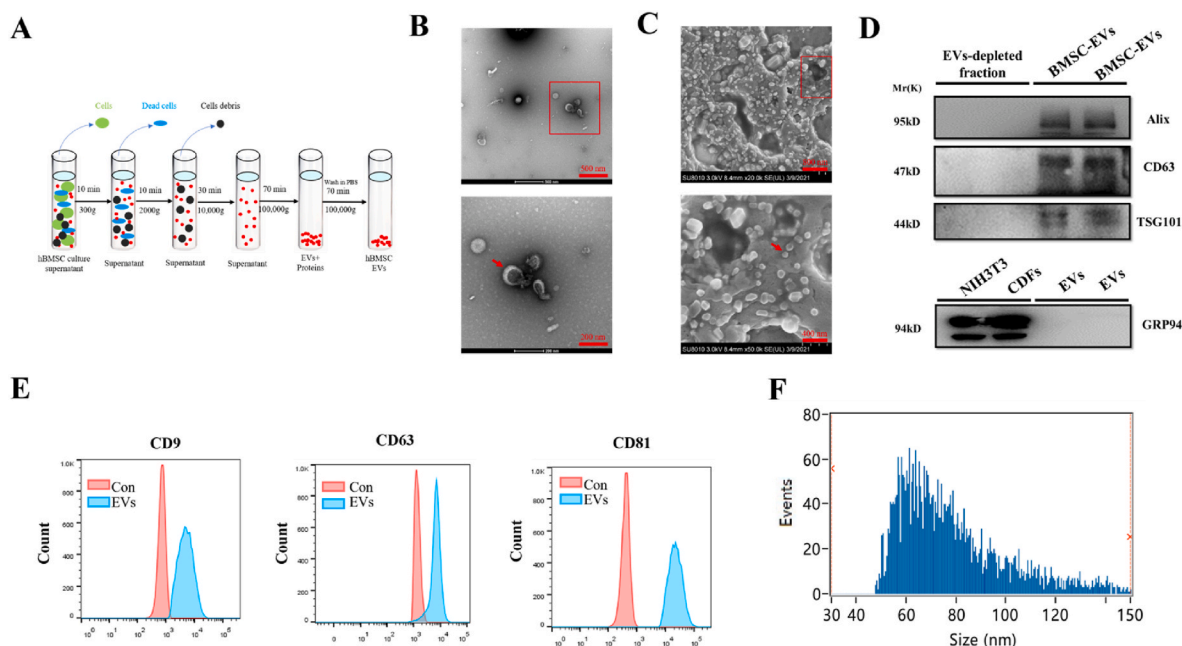


Fig. 1. Identification of hBMSC EVs. (A) The EVs isolation procedures. (B) A representative TEM image of BMSC-EVs, (bar = 500 or 200 nm). (C) A representative SEM image of BMSC-EVs. (D) Protein immunoblots of BMSC-EVs, including four typical exosomal markers (Alix, CD63, and TSG101) and one negative marker (Grp94). The EVs-depleted fraction served as the negative control. (E) Representative flow cytometry plots showing the phenotypes of BMSC-EVs markers, including CD9, CD63, CD81. (F) The particle size distribution of BMSC-EVs was measured.

2.5. BMSC-EVs isolation

The isolation procedures of BMSC-derived EVs were based on the previous study presented in Fig. 1A (Benchtop isolation and characterization of functional EVs by sequential filtration) [20]. In detail, after cells reached 100% confluence, the growth medium was replaced with a fresh exosome-depleted medium (Exosome Depleted Fetal Bovine Serum, ViVaCell, Shanghai, China, C3801-0050). The BMSCs supernatant was harvested after 72hr incubation and subjected to sequential centrifugation (Optima XPN-100 ultracentrifuge; Beckman Coulter SW 41 Ti rotor) to remove the cell debris at 10,000g for 35min and next to remove small cellular debris (12,000g, 45min) at 4 °C. Then, the supernatant was transferred to a new tube and ultracentrifuged (120,000g, 120min) to pellet the small vesicles at 4 °C. Afterward, the precipitate was re-suspended and transferred to a big tube with 50 ml PBS. Hereafter, the EVs-containing PBS was filtered with a 0.22 μm filter to eliminate other contaminants and then ultracentrifuged at 120,000g for 120min. Finally, the EVs were resuspended in exo-free PBS to perform the following experiments or store at −80 °C. The EVs were named BMSC-EVs. The supernatant after pelleting the EVs was collected and named as “EV-depleted fraction”. The EVs extracted from let-7a-5p-knocked-down BMSCs were named “BMSC-EVs^{let-7a-D}”.

2.6. Electron microscope

The EVs were directly observed under a transmission electron microscope (TEM, Tecnai G2 Spirit, Tecnai) and a scanning electron microscope (SEM, MIRA3 FEG-SEM, TESCAN) to evaluate the morphology of EVs. The TEM procedures were based on our previous study [20]. In brief, freshly isolated BMSC-EVs were out on a copper grid coated with 0.125% Formvar in chloroform. Then, 1% (v/v) uranyl acetate in dd-water was applied to stain those grids, and the BMSC-EVs samples were assessed and imaged immediately using the TEM. Additionally, the general procedures of SEM referred to the previous study [42]. In detail, freeze 100 μl BMSC-EVs suspension overnight in the refrigerator at −20 °C, and put it in a vacuum dryer for lyophilization. Then, an appropriate amount of freezing glue was transferred to the sample table

and next the EVs lyophilized powders were spread onto the sample platform. Finally, BMSC-EVs samples were coated with gold by an ion sputterer and observed under the SEM.

2.7. Nanoparticle Tracking Analysis (NTA)

To assess the concentration and absolute size distribution of BMSC-EVs, EVs were analyzed by Flow Nanoanalyzer (High Sensitivity Flow Cytometry for Nanoparticle Analysis, China). Data were collected and processed by the same operator during the whole study, using the software version V1.08, according to the minimal data for studies of EVs (MISEV) [43]. In a nutshell, 10 μl of each BMSC-EVs sample was diluted with PBS based on the detection range (30–150 particles/frame) and then was evaluated by the Flow Nanoanalyzer. Then, the particles were automatically tracked and sized based on Brownian motion and the diffusion coefficient with NTA. The concentration distribution of BMSC-EVs size was shown by NTA software. The NTA software recorded the experiment information with the following laser setting: Min Width: 0.3 ms; 5/40 mW 488; Threshold:75.6 9.8 1.7; Sample pressure: 1.0 Kpa; SS Decay: 10%.

2.8. Flow cytometry Analysis (FACS)

To identify the surface markers of BMSCs, flow cytometry was carried out using the anti-CD34, anti-CD44, anti-CD45, anti-CD31, anti-CD105, anti-CD90, anti-HLA-DR, and anti-CD73 antibodies (above-mentioned antibodies were all purchased from Thermo/eBio, information listed Supplemental Table 3) by Cytomics™ FC 500 (Beckman Coulter). The surface markers of EVs were assessed by flow cytometry analysis using a commercially Exo-Flow capture kit, including CD9, CD63, and CD81 flow antibodies (System Biosciences, CA, USA). The procedures were in line with published study [44]. In brief, isolated EVs were captured by microbead with CD9, CD63, and CD81 antibodies in the kit. Then, stained the Exo-microbead complexes with Exo-FITC, which features FITC bonded to a protein conjugated with the above-mentioned EVs surface protein. Furthermore, the isotype control provided by those kits, which was negative to CD9, CD63, and CD81, was

used as the control group for FACS. Finally, the EV complexes were evaluated and processed by FACS (Novocyte Flow Cytometer, ACEA Bioscience, Inc., MA, USA). In addition, data analysis was conducted using FlowJo software (Version 10).

2.9. *In Vitro* PKH67 tracing for EVs

Isolated BMSC-EVs were labeled with PKH67 using a Green Fluorescent Labeling Kit (Sigma, Aldrich, MINI67-1 KT), and the procedures were according to the company's protocol. In detail, the BMSC-EVs or PBS were stained with PKH67 dye in 500 μ l of Diluent C fluid for 5 min at room temperature (RT). Next, 1 ml 1% BSA was added to stop the labeling process. Then, re-purified BMSC-EVs via ultracentrifugation with PBS rinsing for 30 min. The labeled PBS or BMSC-EVs were co-incubated with human/mice fibroblasts for 12h in a 37 °C, 5% CO₂ cell incubator. Afterward, the culture medium was discarded, and then the dish was washed in PBS three times. Fibroblasts were fixed in 4% PFA and counterstained nuclei with DAPI for 3 min. The endocytosis of the labeled BMSC-EVs by cells was observed by the fluorescence microscope (ECHO Revolve, America). The dye-only group without EVs served as the negative control.

2.10. *In vivo* DIR tracing for EVs

To visualize the target tissue (shoulder capsular) of EVs *in vivo*, BMSC-EVs were labeled with DIR (1,1-dioctadecyl-3,3,3,3-tetramethylindotricarbocyanine iodide) (D12731, Invitrogen, Life Technologies) according to the manufacturer's instructions. In general, 100 μ g of BMSC-EVs were incubated with DIR (1:1000 in PBS) in the darkness for 15 min, and then the labeled BMSC-EVs were washed in 40 ml PBS, with centrifugation at 120,000 g for 100 min to avoid the excess dye. After then, the DIR-labeled EVs were injected into the shoulder joint cavity of C57/6J mice (8 weeks old, dosage: 100 μ g of EVs/150 μ l of PBS), and PBS without DIR was used as the control group. After 1h, 3d, or 7d, the mice were subject to *in vivo* imaging. Finally, fluorescence intensity was evaluated by the IVIS software (Living Image Software for IVIS).

2.11. Establishment of mice SS model and Treatment

In this study, ~12-week-old Male C57/6J mice were utilized and the SS model was established via an immobilization procedure on the left shoulder that the scapula of the mouse was firmly tied to the distal third of the humerus by braided polyester sutures [45,46]. The sham procedure was performed on negative control (NC group), while the immobilization experiment group was named SS group. 21 days after SS model establishment, sutures were removed and different treatments began. Intra-articular injection of 50 μ l EV (20 μ g/ml or 50 μ g/ml, equal to final particle from 1.2×10^8 to 3×10^8 , EVs were intra-capsular injected every 7 days for a total of three injections), or 10ul miRNAs agomir (10 nmol in 10ul) (miRNAs agomir were purchased from RiboBio, China) was administrated using micro-syringe once a week for three weeks (Sequence listed in Table S1). Six mice were randomly allocated per group and all the animals were allowed to move freely in the cages after surgery under a 12h light-dark circle condition. Based on our preliminary experiments, five mice were required to reach a statistical significance between the NC group and SS group regarding the difference of ROM, thus six mice were randomly allocated into each group.

2.12. Animal/patients shoulder sample harvest and analysis

Six weeks after immobilization, all the mice were euthanized by overdose CO₂ to harvest the left shoulders. Passive ROM was measured using the method reported by Oki et al. [47] immediately after sample collection. Next, the samples were fixed in 8% PFA for one day, and were decalcified, dehydrated, and embedded in paraffin wax for further histological evaluation. The thickness of the joint capsule was recorded by

six random measurements using ImageJ 7.0 software to obtain a mean value. The relative thickness of joint capsules of different groups compared to that of the NC group was calculated. The analysis above was conducted by the third author unaware of mice treatments. The patient's samples were collected during surgery and immediately embedded in OCT at -80 °C for further study.

2.13. Histological analysis

2.13.1. Hematoxylin and eosin (HE) staining

The method of HE was based on the published study [48]. Briefly, the embedded joint capsules were cut into 6 μ m thick sections by a paraffin slicing machine (LEICA RM2235). Next, sections were dewaxed and rehydrated with gradient xylene/alcohol and PBS. Hematoxylin and eosin-stained were performed on the tissue separately for 10 min and 1 min. Finally, the tissue was sealed with neutral resin and directly observed under the microscope (ECHO Revolve, American).

2.13.2. Masson staining

The cutting, dewaxing, and rehydration procedures were the same as those in HE stains. The whole process was according to the commercial kit for Masson staining (Solarbio, China). The sections were observed and pictured by the microscope (ECHO Revolve, American). The thickness of all the joint capsules was measured. In addition, the cell number of the shoulder capsule was counted in a 25 μ m*25 μ m area (five values were counted for one sample).

2.14. Immunohistologic analysis

As mentioned above, the capsule samples were cut into 6 μ m thick slices. Then sections were dewaxed and rehydrated with gradient xylene/alcohol and PBS. The water surrounding the capsule was cleaned up, and circles were drawn on each tissue using a fluorescent pen. Capsule slices were then blocked in 5% BSA and 0.5% Triton-X-100 (Solarbio, Beijing, China) for 1 h at RT. Afterward, they were incubated with primary antibodies overnight at 4 °C. Next, 1 \times TBST washing for 5 min three times was performed before and after incubation with Alexa Fluor 488 anti-mouse (H + L) secondary antibodies (1:500; Life Technologies, USA) for 1 h at RT. Finally, images were pictured by the immunofluorescence microscope (Olympus, X71).

As for cell immunofluorescence staining, CDFs or NIH3T3 were seeded on glass slides and incubated in high-glucose DMEM until 30%–50% confluent. After that, different treatments were performed with serum-free DMEM. Next, after being washed with PBS, cells were fixed with 4% paraformaldehyde for 10 min followed by permeabilization in PBS with 0.5% Triton-X-100 for 10 min and 5% BSA blockage for 60 min at RT. After then, immunofluorescence was performed with primary antibodies incubation at 4 °C overnight, and next with the corresponding secondary antibody for 1 h at RT. DAPI was used to counterstain the nuclei. Finally, images were pictured by the immunofluorescence microscope (Olympus, X71).

2.15. BrdU

The proliferation of CDFs or NIH3T3 was evaluated using a 5-Bromo-2'-deoxyuridine (BrdU) incorporation assay kit (Cell Signaling Technology, MA, USA) following the manufacturer's instructions. In brief, CDFs or NIH3T3 were seeded into a 6-well plate with 1×10^6 cells/well and they were treated with different interventions for 24h. Then, BrdU solution was added into each well for another 12 h after interventions. Next, cells were fixed and washed with PBS and incubated with mouse anti-BrdU-primary antibody for 1h at RT. Finally, DAPI was used to counterstain the nucleus for 3 min. Cell proliferation was measured using the average number of BrdU + cells/number of DAPI per mm².

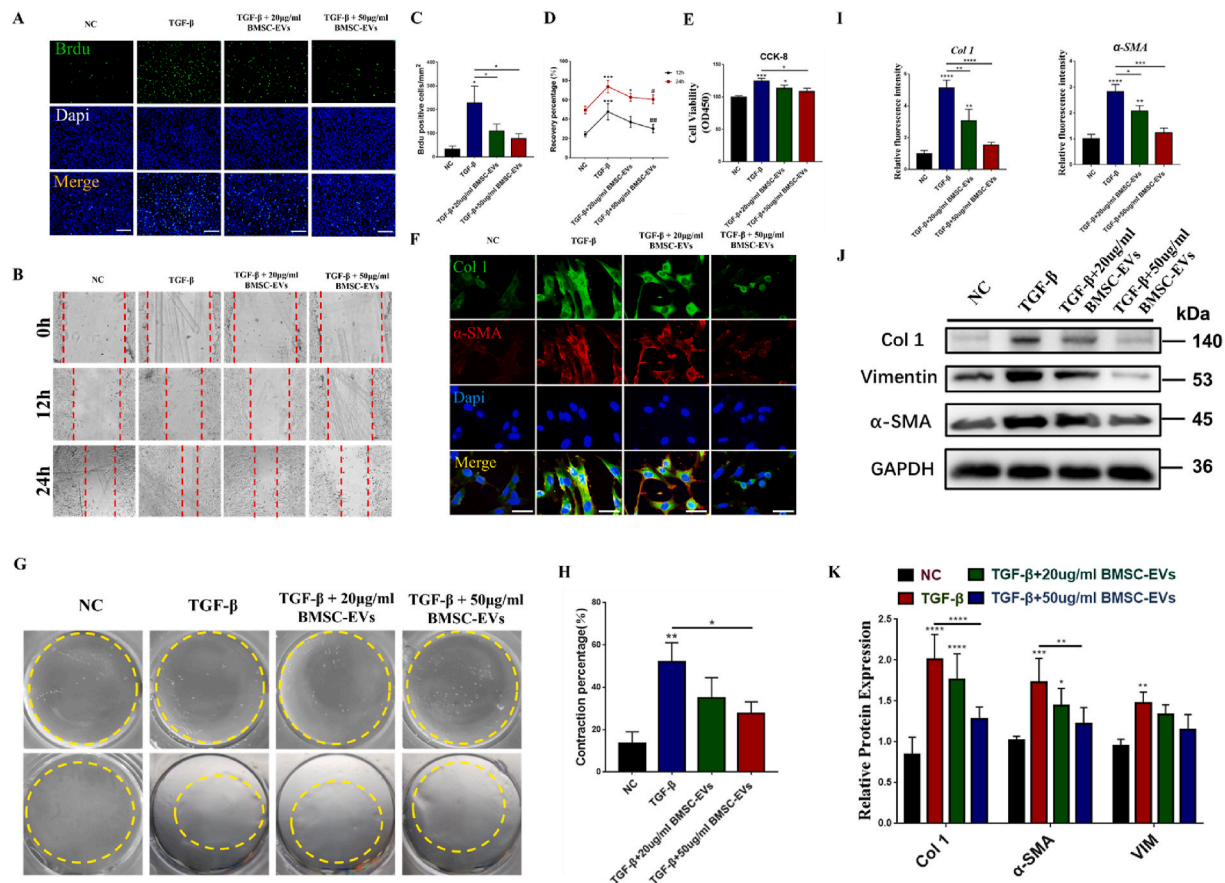


Fig. 2. BMSC-EVs relieved CDFs fibrogenesis induced by TGF- β *in vitro*. (A) Cell proliferation ability of CDFs was determined using BrdU incorporation assay after TGF- β stimulation with or without 20 μ g/ml BMSC-EVs and 50 μ g/ml BMSC-EVs incubation for 24h. Green signal = BrdU. Scale bar = 180 μ m. (B) The cell migration ability of CDFs was determined by wound-healing assay after 12h and 24h incubation with different treatments. (C–D) Quantification of BrdU and wound-healing data (n = 3). Data are presented as mean \pm SD. *P < 0.05, ***P < 0.001, # < 0.05, ##P < 0.01, # compared with TGF- β group. (E) Cell proliferation ability of CDFs was further determined using CCK-8 assay. (n = 4) Data are presented as mean \pm SD. *P < 0.05, ***P < 0.001. (F) Immunofluorescence was used to detect relative expression and distribution of α -SMA and Collagen 1 with different treatments. Green, red, and blue signal represented Collagen 1, α -SMA, and nucleus, respectively. Scale bar = 25 μ m. (G) The representative image of the ability of collagen contraction of CDFs in different groups (yellow dotted line indicated the collagen gel). (H) The relative quantification of the area of collagen gel in different groups compared to that of group NC at 24h. (n = 3) Data are presented as mean \pm SD. *P < 0.05, **P < 0.01. (I) Relative fluorescence intensity of Col 1 and α -SMA after different treatments. (n = 3) Data are presented as mean \pm SD. *P < 0.05, **P < 0.01, ***P < 0.001, ****P < 0.0001. (J) Collagen 1, Vimentin and α -SMA protein levels in CDFs were presented by western blot after different treatments. (K) Quantification of western blot data (n = 4). Data are presented as mean \pm SD. *P < 0.05, **P < 0.01, ***P < 0.001, ****P < 0.0001.

2.16. Wound healing assay

To evaluate the cell migration ability of CDFs or NIH3T3 fibroblasts, an *in vitro* scratch assay was performed by scratching a straight line in the middle of the 24-h cultured cell plate with 80% confluence. Next, different treatments were performed for another 24h, and the culture dishes were observed/pictured under an inverted microscope. Cell migration ability under different conditions was assessed by the recovery rate (The migrated distance/the original wound distance \times 100%).

2.17. CCK-8 assay

Cell counting kit-8 (CCK-8, Beyotime Biotechnology, Shanghai, China) assay was utilized to evaluate the viabilities of CDFs or NIH3T3 after different interventions. The general procedures were based on the previous study [49]. Briefly, CDFs or NIH3T3 were seeded into a 96-well plate (Thermo Fisher Scientific, MA, USA) with 1×10^3 cells/well and treated by different interventions for 24 h. Then, 10 μ l CCK-8 solution was added to each well, and the plate was incubated for 2 h and measured with the absorbance (450 nm) by Microplate Reader (Bio-Rad, Hercules, CA, USA). Cell viabilities were assessed by average absorbance of different interventions/absorbance of control group \times 100%.

2.18. Collagen contraction test

A collagen contraction experiment was performed as described previously [41]. In general, CDFs (2.0×10^5 cells/ml) were suspended in 24-well plates with a 1 ml growth medium, which contained 300ul of 2 mg/ml concretionary collagen (Solarbio, Beijing, China) with or without other substances, such as TGF- β and EVs in each well. Besides, collagen was detached from the well using 100 μ l-sterile pipette tips. Then, the plates were put into a 37 $^{\circ}$ C incubator with 5% CO₂, and digital photos were pictured by screening at 0 and 24 h. Finally, contraction of the collagen was measured by ImageJ software (NIH, Bethesda, MD, USA) to evaluate the relative-contraction ratio compared to the NC group.

2.19. Western blot

Isolated BMSC-EVs were assessed for the presence of exosomal markers, including Alix, CD9, CD63, and HSP60 as previously described (the information of antibodies was recorded in Table S3). The EVs-depleted fraction from cell supernatant served as negative control and the Grp94 protein, which is present only in large vesicles but not in EVs (< 200 nm), was utilized to verify the purity of EVs. The other western blot procedures were according to the previous study [50]. Proteins

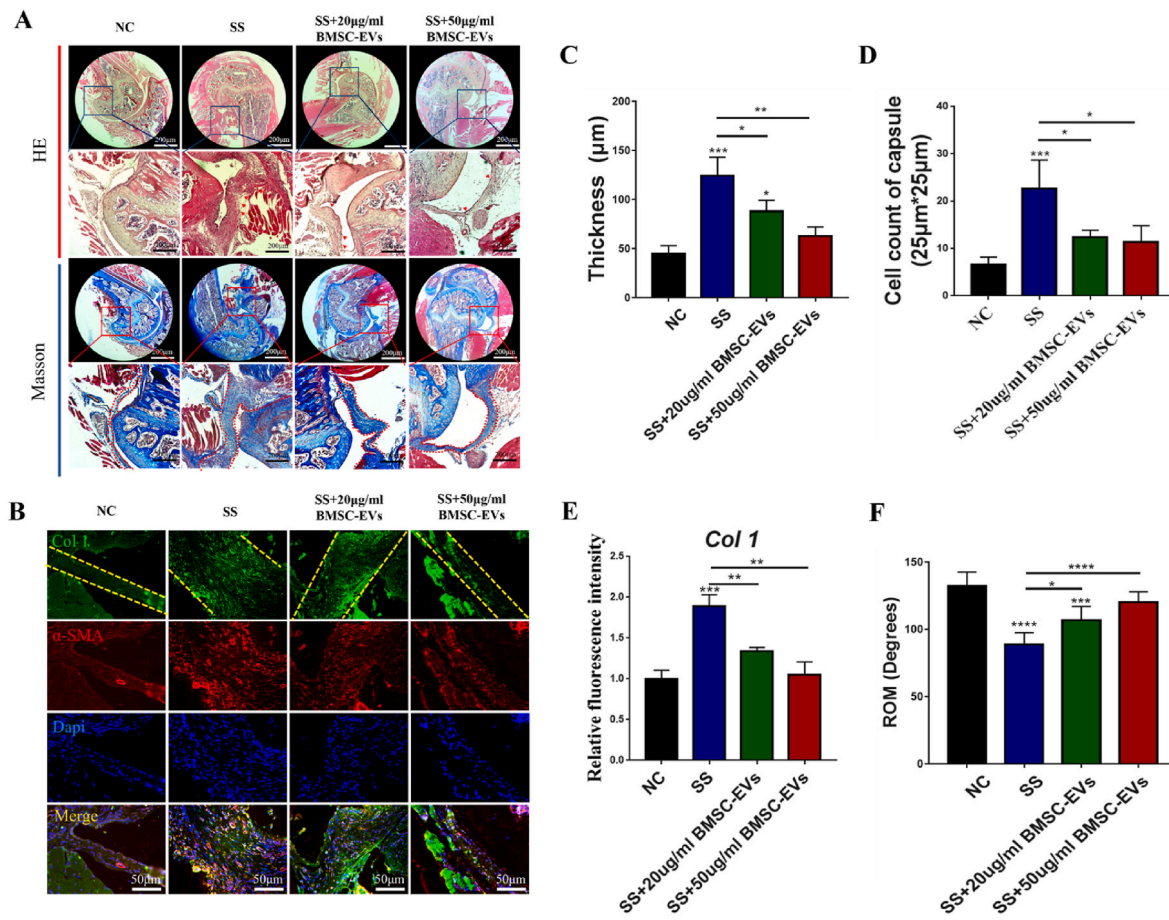


Fig. 3. The impact of different concentrations of BMSC-EVs on the histological and biomechanical appearance of mice shoulders with immobilization. (A) The representative image of the joint capsule of the shoulder on HE staining and Masson staining. Scale bar = 200 μm. The red arrow indicated the hypercellular status of the joint capsule. The red dotted line indicated the inner and outer border of the joint capsule. (B) Representative immunofluorescence images showed the protein and relative expression of α-SMA and Collagen 1 in the mice capsular samples. Scale bar = 50 μm. (C) Quantification of capsule thickness and inter-group comparison. (n = 3) *P < 0.05, **P < 0.01, ***P < 0.001. (D) Cell number of shoulder capsule was counted. (n = 3) *P < 0.05, ***P < 0.001. (E) Relative fluorescence intensity of α-SMA with different treatments. (n = 3) **P < 0.01, ***P < 0.001. (F) Quantification of passive range of motion. (n = 6) *p < 0.05, ***p < 0.001, ****p < 0.0001. Data are presented as mean ± SD.

were extracted from BMSC-EVs or cells with RIPA buffer (R0010; Solarbio, China) containing Phenyl methane sulfonyl fluoride (PMSF; Solarbio, China). Next, the concentrations of protein were measured using the BCA Protein Assay Kit (Beyotime Biotechnology, China). Then protein samples (10 μg) were separated by 10% SDS-PAGE and transferred to nitrocellulose membranes by normal procedures. Afterward, the blots were blocked with PBST containing 5% non-fat milk for 1 h before applying primary antibodies at 4 °C overnight (Table S3). After then, peroxidase-conjugated secondary antibodies were incubated with blots at 1:2000 for 1 h at RT. Last, all protein bands were observed, pictured, and analyzed by an SYNGENE imaging system (Cambridge, UK) and ImageJ (NIH, Bethesda, MD, USA). Four protein samples per group were used for calculation (n = 4/group).

2.20. Exosomal microRNAs sequencing

Small-RNA sequencing was performed using a commercial service (Personal Biotechnology Co., Ltd. Shanghai, China). In brief, total RNAs were extracted from three groups of BMSC-EVs using the miRNA easy Kit (Qiagen, Hilden, Germany), and the quality/concentration of the RNAs were assessed by Qubit (Life Technologies, USA) Agilent 2200. After reverse-transcription-PCR amplification, small-RNA libraries were established and sequenced with raw reads being collected by an Illumina HiSeq 2500 platform. $|\log_2(\text{fold change})| \geq 1$ plus $P < 0.05$ was considered as differentially expressed.

2.21. Real-time quantitative polymerase chain reaction (qPCR)

To evaluate the level of mRNAs and miRNAs in cells, total RNA was extracted from cells by Trizol reagent (Invitrogen) and quantified by Nanodrop (Thermo Scientific, Waltham, USA). Stem-loop qPCR (Taq-Man) was applied to measure the expression of miRNAs (let-7a-5p, let-7a-3p, let-7b-5p, and let-7b-3p) as previously mentioned using U6 as reference. To evaluate mRNA levels, the cDNA was used as the template for qPCR with TB Green™ Premix Ex Taq™ II (Takara; RR820A) with GAPDH as reference. Besides, the miRNA and mRNA qPCR primer sets were obtained from RiboBio, and mRNA qPCR primers were synthesized by Sangon (Shanghai, China). Table S2 showed the qPCR primers applied and Table S1 presented the sequences of miRNA and siRNA in the current study. The comparative Ct method ($2^{-\Delta\Delta Ct}$) was applied to calculate the value of each sample, which was performed in triplicate. Finally, we normalized all values by NC group.

2.22. Bioinformatic analysis and target gene prediction

Total small RNA constitution analysis for known/unknown RNA, miRNA Upset analysis, CPM gene expression density distribution, and correlation analysis of samples were conducted to verify the miR quality and consistent between three BMSC-EVs samples. Gene Ontology (GO) and KEGG pathway enrichment analysis and annotation were performed by DAVID bioinformatics tool for top-200 high expressed miRs.

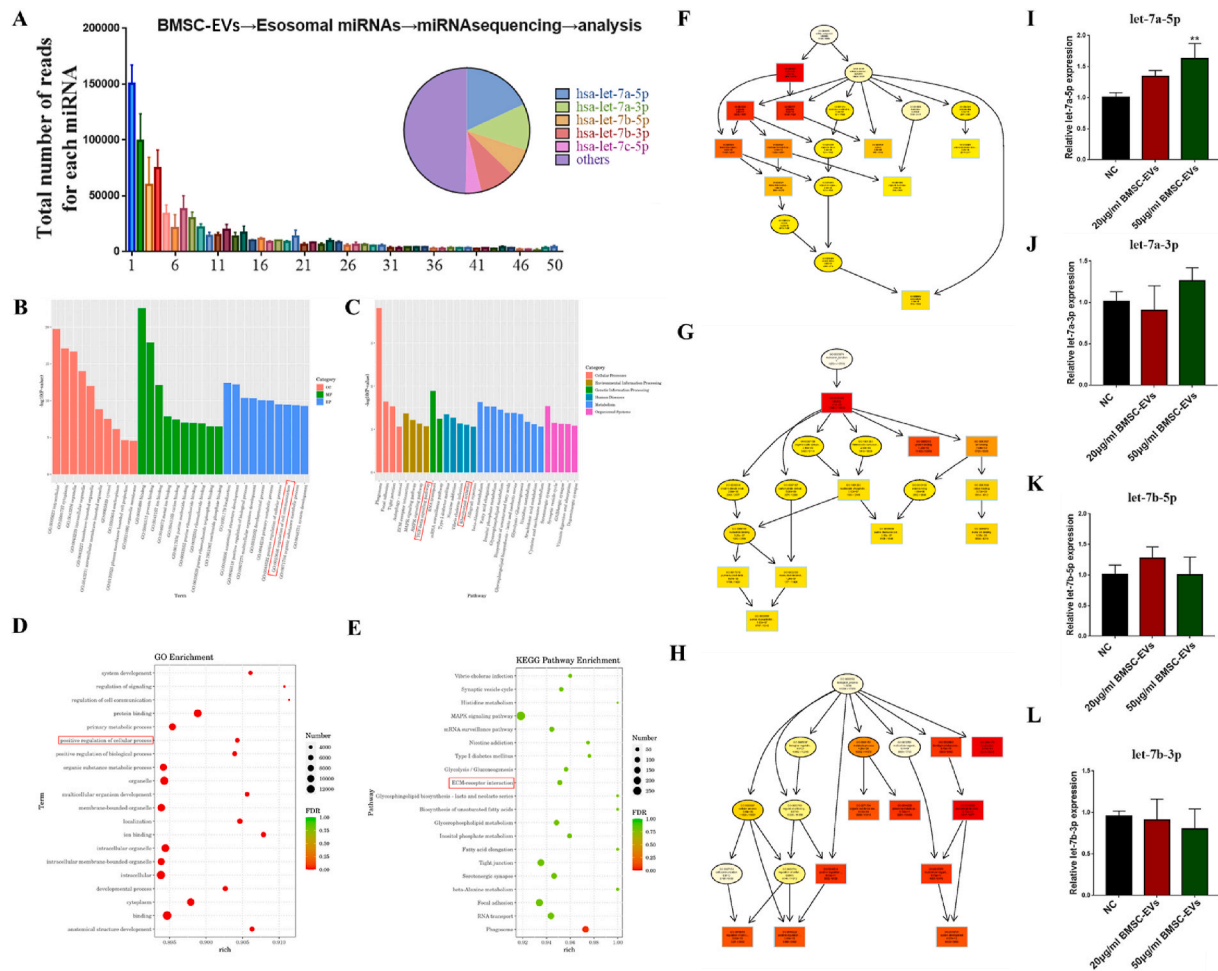


Fig. 4. Small RNA sequencing, GO/KEGG analysis, and verification of the expression of miRNAs. (A) Histogram and pie chart of miRNAs highly expressed in BMSC-EVs. The top 5 expressed miRNAs were presented. (B) GO enrichment was analyzed for Top-200 expressed miRNAs in BMSC-EVs, including functional pathways, Biological processes, Cellular components. (C) KEGG enrichment was analyzed for Top-200 expressed miRNAs in BMSC-EVs, including Environmental information processing, Human diseases, Metabolism, and so forth. (D) Bubble plot showing GO enrichment by Top-200 expressed miRNAs targeted in functional pathways, Biological Process, Cellular Component. (E) Bubble plot showing KEGG enrichment by Top-200 expressed miRNAs targeted in functional pathways. (F–G) Three directed acyclic graphs further analyzed the TOP-10 activities of biological processes, molecular functions, and cellular components for Top-200 expressed miRNAs. (I–L) High expression levels of let-7a-5p, let-7a-3p, let-7b-5p, and let-7b-3p in CDFs after different concentration of BMSC-EVs were confirmed using qPCR. (n = 3) Data are presented as mean ± SD. **P < 0.01.

Targetminer, miRWalk, starBase, and mirDIP online databases were applied for miRNA target-gene prediction.

2.23. Dual-luciferase reporter assay

CDFs were co-transfected with luciferase vectors containing wild-type or mutant 3'-UTR of TGFBRI1, and miR-let-7a-5p mimics or mimics-NC by using Lipofectamine 3000 (Invitrogen). Luciferase activities were measured using a Dual-Luciferase Reporter Assay System (Beyotime) after 48 h-transfection.

2.24. Statistical analysis

All experiments in this study were conducted at least three times. Data were analyzed using GraphPad Prism 7.0 (GraphPad Software, La Jolla, CA) and were presented as mean ± SD. Mann–Whitney *U* test, non-parametric Student *t*-test, one/two-way analysis of variance (ANOVA), or analysis of variance, followed by post hoc Bonferroni test were applied to evaluate the differences between groups, based on the normal distribution of data or not. P < 0.05 was regarded as significant.

3. Results

3.1. Identification of induced differentiation ability and biological properties of BMSC

To identify the BMSCs' property, several experiments were performed. First, BMSCs presented a homogeneous population of spindle fibroblast-like cells, which is consistent with previous studies (Supplemental Fig. 2A). Besides, those cells positively expressed CD105, CD44, CD90, and CD73 and negatively expressed CD34, CD31, HLA-DR, and CD45 by flow cytometry (Supplemental Fig. 2B). Moreover, biological effectiveness experiments suggested that BMSCs could be differentiated into adipogenic, osteogenic, and chondrogenic phenotypes shown by different kinds of staining, whereas control groups did not show those phenomena (Supplemental Figs. 2C–E).

3.2. Identification and characterization of BMSC-EVs

Under transmission and scanning electron microscopy, BMSC-EVs presented a typical goblet or spherical shape (Fig. 1B and C). Western blot results suggested that exosomal marker proteins (Alix, TSG101, and CD63) were highly expressed in EVs, whereas these proteins were not

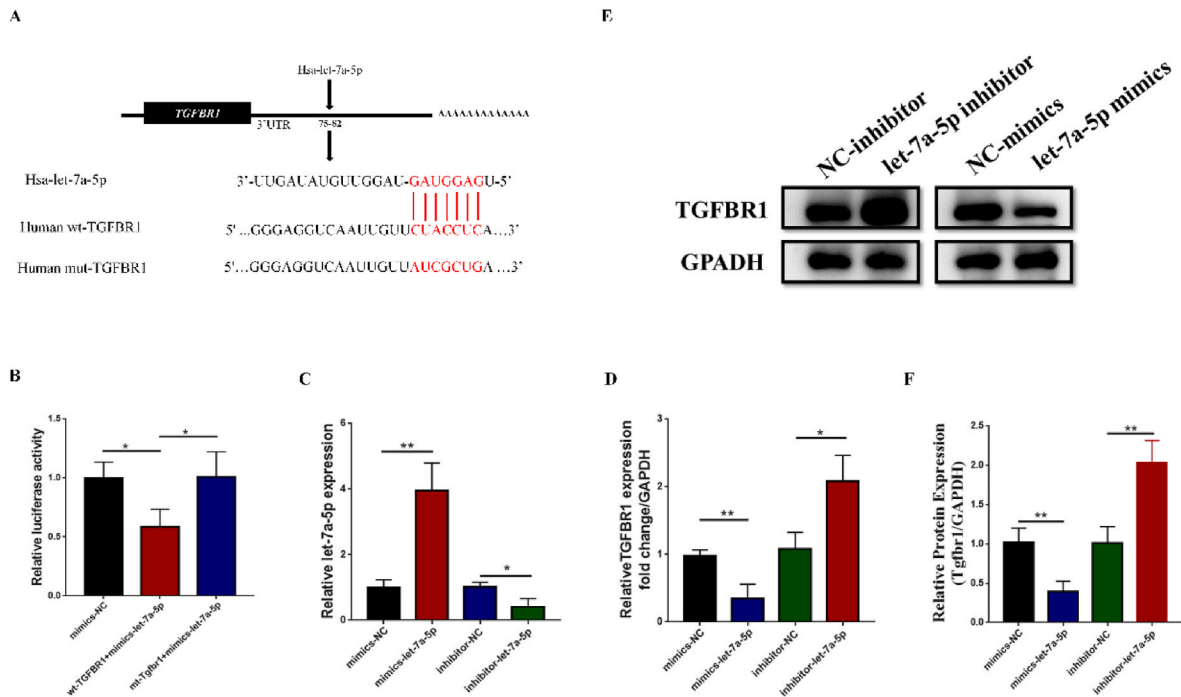


Fig. 5. TGFBR1 was the direct target of let-7a-5p. (A) The putative let-7a-5p binding sequence in the 3'-UTR of TGFBR1 mRNA. The mutation was generated in the TGFBR1 3'-UTR sequence in the complementary site of the let-7a-5p seed region. (B) Suppressed luciferase activity of wild-type TGFBR1 3'UTR by let-7a-5p mimic. CDFs were co-transfected with pGL3-TGFBR1-3'UTR or pGL3-TGFBR1-3'UTR-mut, and let-7a-5p mimic or NC duplex. Firefly luciferase activity of each sample was measured 48 h after transfection and normalized to control luciferase activity. (n = 3) Data are presented as mean \pm SD. *P < 0.05, **P < 0.01. (C) The let-7a-5p gene expression level was assessed by qPCR. U6 served as an internal parameter. (n = 3) Data are presented as mean \pm SD. *P < 0.05, **P < 0.01. (D–F) Gene and protein expression of endogenous TGFBR1 is regulated by let-7a-5p. The expression level of endogenous TGFBR1 in CDFs was determined 48h after transfection with let-7a-5p mimic, let-7a-5p inhibitor, or NC duplex by qPCR and Western blotting. GAPDH was used as an internal control. (n = 3) Data are presented as mean \pm SD. *p < 0.05, **P < 0.01.

detected in EVs-depleted fraction (Fig. 1D). In addition, the Grp94 protein was only detected in NIH3T3 and CDF fibroblasts rather than in EVs, which indicated EVs in this study were pure enough (Fig. 1D). Besides, flow cytometry results indicated that exosomal markers (CD9, CD63, and CD81) were highly expressed in BMSC-EVs (Fig. 1E). Moreover, NTA results showed that the diameters ranged from 30 to 150 nm (Fig. 1F), and the percentage of molecules in this range is 94.92% with a mean of 78.64 ± 21.72 nm and a median of 73.25. In addition, the original concentration of BMSC-EVs is 1.13×10^{10} /ml. The detailed data and reports were provided in the supplemental material.

3.3. BMSC-EVs inhibit TGF- β induced fibrogenesis *in vitro*

The functions of BMSC-EVs were evaluated. BMSC-EVs could be internalized by CDFs from the RCT cohort and NIH3T3 (Supplemental Fig. 3). TGF- β is a powerful pro-fibrotic factor in the joint capsule of stiffened shoulder and was highly expressed in our samples of the SS group compared to the RCT group (Supplemental Fig. 4). Thus, for experiments *in vitro*, we utilized this factor to mimic the extracellular environment of fibrosis *in vivo*. We found that BMSC-EVs significantly inhibited TGF- β induced enhanced CDFs activity, as presented by BrdU staining, wound healing assay, and CCK-8 assay (Fig. 2A to E) in a concentration-dependent manner. In addition, collagen contraction analysis further demonstrated that BMSC-EVs inhibited CDFs mediated collagen contraction induced by TGF- β intervention (Fig. 2G and quantified in 2H). Similarly, immunofluorescence staining (Fig. 2F, quantified in Fig. 2I) and western blot (Fig. 2J, quantified in Fig. 2K) detected a significant decrease of Col 1, α -SMA, and VIM protein expression caused by EVs in CDFs stimulated with TGF- β , suggesting an anti-fibrotic effect of BMSC-EVs.

To make the above results more convincing, NIH3T3 fibroblasts were

utilized to evaluate the effect of BMSC-EVs on fibrotic phenotypes. After proving that BMSC-EVs could be successfully captured and internalized by NIH3T3 cells (Supplemental Fig. 3), BrdU staining, wound healing assay, and CCK-8 assay indicated the pro-fibrotic activities or migration ability of NIH3T3 were suppressed by BMSC-EVs (Supplemental Figs. 5A–5E). Additionally, immunofluorescence showed BMSC-EVs could inhibit TGF- β induced Col 1 and α -SMA expression in a concentration-dependent manner (Supplemental Fig. 5F and quantified in 5G).

Meanwhile, the influence of BMSC-EVs on CDFs from patients with stiffness was assessed. BrdU staining, wound healing assay, and CCK-8 assay indicated the pro-fibrotic activities or migration ability of CDFs were suppressed by BMSC-EVs (Supplemental Figs. 6A–6E). In addition, immunofluorescence showed BMSC-EVs could inhibit Col 1 and α -SMA expression in a concentration-dependent manner (Supplemental Fig. 6F and quantified in 6G).

3.4. BMSC-EVs suppress frozen shoulder in a mouse model

Afterward, the effects of BMSC-EVs on fibrosis *in vivo* were investigated in a mouse model of SS. Our preliminary results suggested that the ROM of the immobilized shoulder in our animals decreased gradually in the first 3 weeks after surgery and then stayed in a stable plateau (Supplemental Fig. 7). Thus, three weekly intra-articular injections of BMSC-EVs into the mice's index shoulder were performed on day 22 after immobilization. 21 days after the first injection procedure, shoulder samples were harvested. Besides, the shoulder capsular samples from SS patients highly expressed the Col 1 and α -SMA proteins (Supplemental Fig. 8), which suggested they could be utilized as fibrotic markers for SS. The EVs tracing results showed that BMSC-EVs were properly injected in the shoulder joint cavity of mice and BMSC-EVs can

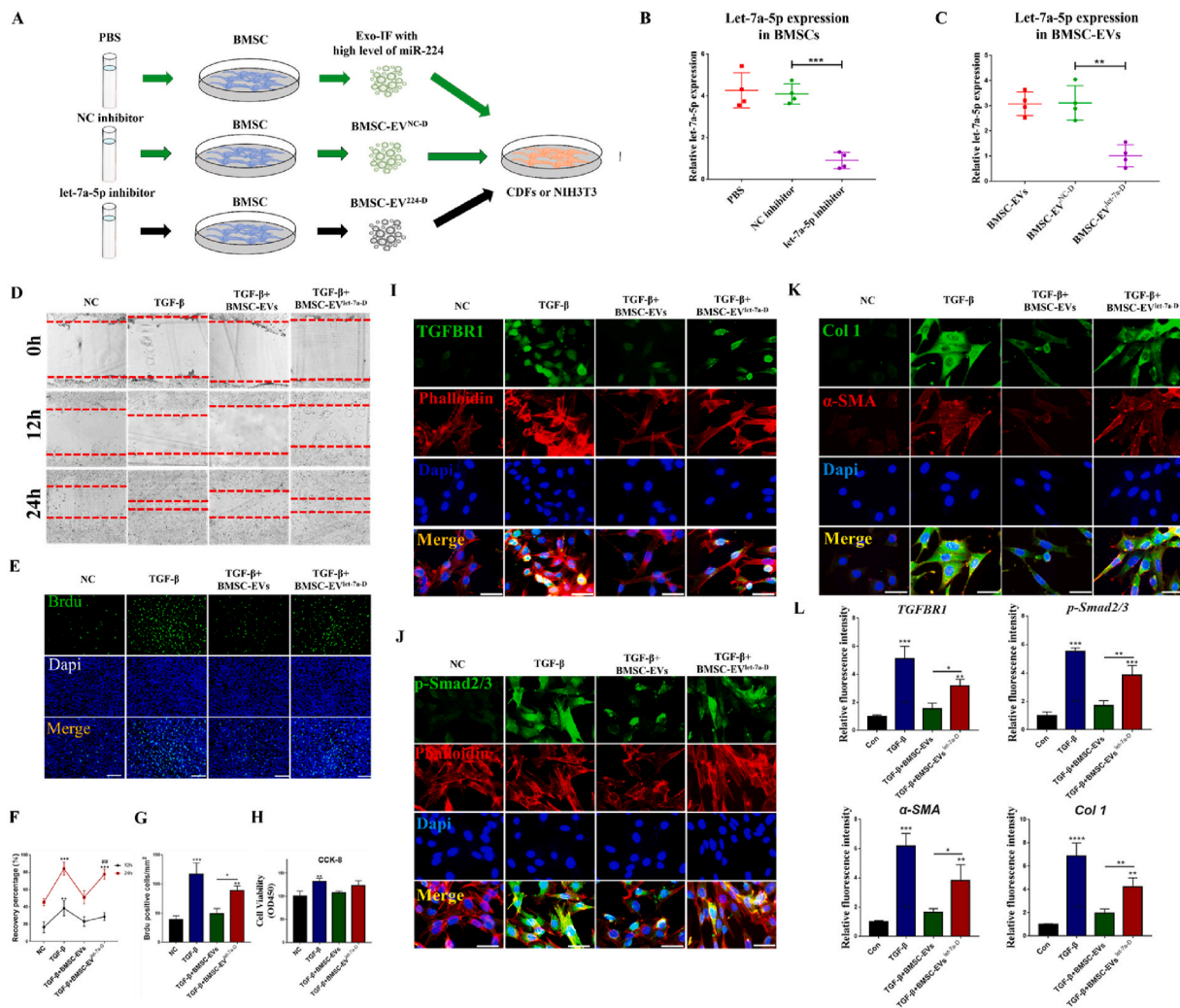


Fig. 6. The anti-fibrotic effects of BMSC-EVs relied on let-7a-5p. (A) Schematic diagram of different treatments for BMSCs and their corresponding EVs. (B–C) The let-7a-5p gene expression levels in BMSCs or EVs were assessed by qPCR. (n = 3) Data are presented as mean ± SD. **P < 0.01, ***P < 0.001. (D) The cell migration ability of CDFs was determined by wound-healing assay after TGF-β, TGF-β+BMSC-EVs, or TGF-β+ BMSC-EVs^{let-7a-D} for 24h. (E) Cell proliferation ability of CDFs was determined using BrdU incorporation assay after different treatments for 24h. Green signal = BrdU. Scale bar = 180 μm. (F–G) Quantification of wound-healing assay BrdU assay data (n = 3). Data are presented as mean ± SD. *P < 0.05, **P < 0.01, #P < 0.05, # compared with NC inhibitor group (H) Cell proliferation ability of CDFs was further determined using CCK-8 assay. (n = 3) Data are presented as mean ± SD. *P < 0.05. (I) Immunofluorescence was used to detect relative expression and distribution of TGFBR1 with different treatments. Green, red, and blue signals represented TGFBR1, Phalloidin, and nucleus, respectively. Scale bar = 50. (J) Immunofluorescence was used to detect relative expression and distribution of p-Smad2/3 after different treatments for 24h. Green, red, and blue signals represented p-Smad2/3, Phalloidin, and nucleus, respectively. Scale bar = 25 μm. (K) Immunofluorescence was used to detect relative expression and distribution of Col 1 and α-SMA after different treatments for 24h. Green, red, and blue signals represented Col 1, α-SMA, and nucleus, respectively. Scale bar = 25 μm. (L) Relative fluorescence intensity of TGFBR1, p-Smad2/3, Col 1, and α-SMA with different treatments. (n = 3) Data are presented as mean ± SD. *P < 0.05, **P < 0.01. ***P < 0.001.

exist at the cavity for 7 days (Supplemental Fig. 9). In addition, HE staining results for organs indicated that the structures of the heart, kidney, liver, spleen, lung, and intestine were not changed by BMSC-EVs injection (Supplemental Fig. 10), which generally demonstrated the safety of BMSC-EVs administration. Additionally, HE staining for shoulder samples showed that no matter immobilized shoulders were administrated to BMSC-EVs injection or not, cell infiltration in the capsule was more severe than in that of the NC group (Fig. 3A and quantified in 3D). Besides, Masson staining further indicated that the thickness of the capsule in the SS group and two SS groups with different concentrations of BMSC-EVs injection was significantly higher than the shoulder capsular of the NC group. But the thickness of SS + BMSC-EVs groups was significantly lower than that of the SS group, suggesting an anti-fibrotic potential of BMSC-EVs (Fig. 3A and quantified in 3C). As for immunohistology, the expression and space of either Col 1 or α-SMA remarkably accumulated and occupied in the capsule of three SS groups

than of NC group, while this accumulation was remarkably lower in SS + BMSC-EVs groups than that of the SS group (Fig. 3B and quantified in 3E). Meanwhile, the ROM of the SS + BMSC-EVs group was significantly higher compared with that of the SS group (Fig. 3F). Taken together, BMSC-EVs owned anti-fibrotic potential both *in vitro* and *in vivo*.

3.5. Let-7a-5p is highly expressed in BMSC-EVs

To discover the BMSC-exosomal miRNAs that were responsible for its anti-fibrotic effects, exosomal miR sequencing was performed in three groups of BMSC-EVs. The quality and consistency between each sample were verified by different methods (Supplemental Figs. 11A–F). Top ten expressed miRNAs were detected, i.e., let-7a-5p, let-7a-3p, let-7b-5p, and let-7b-3p (Fig. 4A). GO analysis indicated that various biological processes, molecular functions, and cellular components were engaged in miR-related functions (Fig. 4B and D, analyzed detailedly in

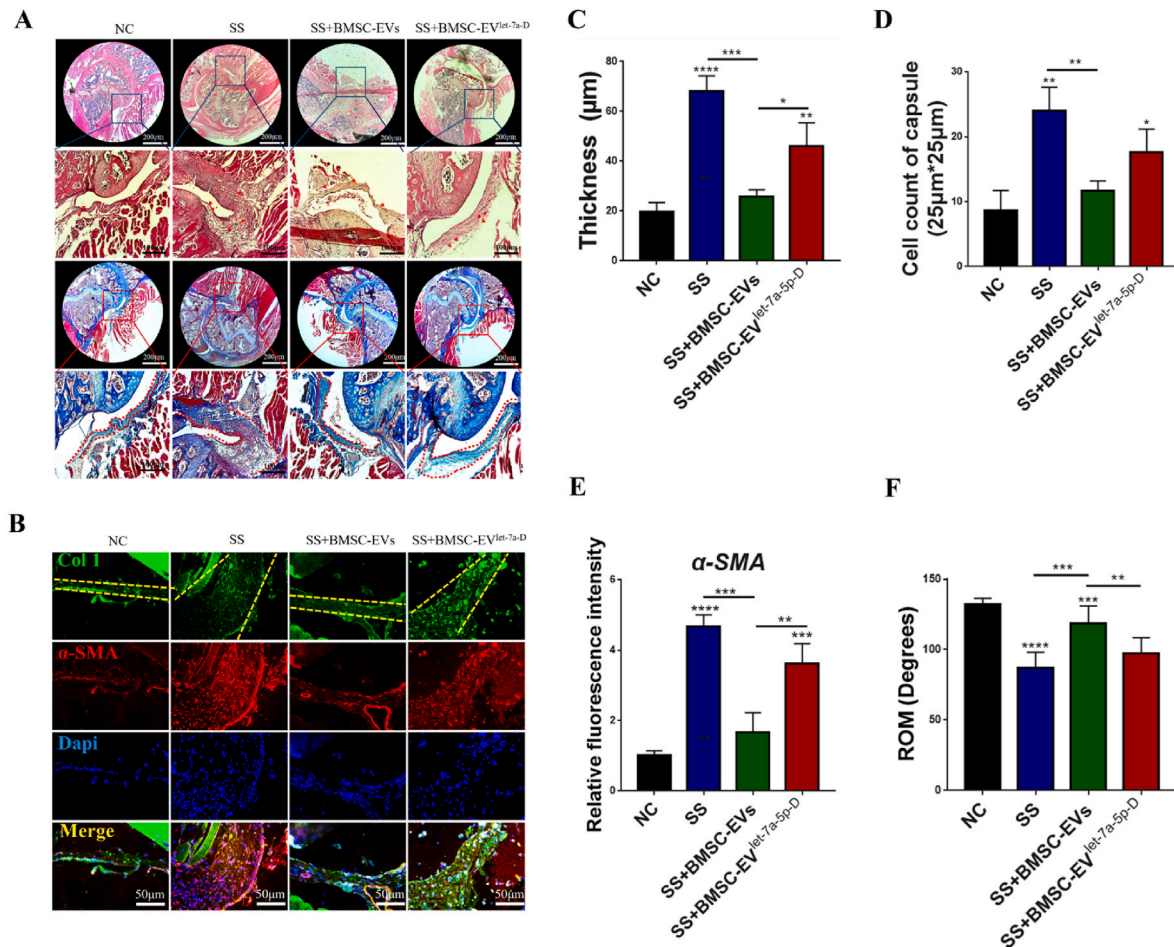


Fig. 7. The impact of BMSC-EVs on the histological and biomechanical appearance of mice shoulders with immobilization after let-7a-5p-knockdown. (A) The representative image of the joint capsule of the shoulder on HE staining and Masson staining. Scale bar = 200 or 100 μm. The red arrow indicated the hypercellular status of the joint capsule. The red dotted line indicated the inner and outer border of the joint capsule. (B) Representative immunofluorescence images showed the location and relative expression of Collagen 1 and α-SMA in the mice capsular samples. Scale bar = 50 μm. (C) The quantification of capsule thickness and inter-group comparison. (n = 3) *P < 0.05, **P < 0.01. (D) Cell number of shoulder capsule was counted. (n = 3) *P < 0.05, **P < 0.01. (E) Relative fluorescence intensity of α-SMA with different treatments. (n = 3) **P < 0.01, ***P < 0.001, ****P < 0.0001. (F) Quantification of passive range of motion. (n = 6) *p < 0.05, **P < 0.01. ***P < 0.001. Data are presented as mean ± SD.

Supplemental Fig. 11G–L). In addition, three directed acyclic graphs further analyzed the TOP-10 activities for biological processes, molecular functions, and cellular components (Fig. 4F to H). Moreover, using KEGG analysis, several signaling pathways were identified, among which the TGF-β signaling pathway, the well-known pro-fibrotic signaling pathway, was noted (Fig. 4C and E). These activities underlined a deep enrollment of BMSC-EVs in the anti-fibrotic process. Furthermore, PCR showed that let-7a-5p was significantly expressed in CDFs after different concentrations of BMSC-EVs treatment, while the other three let-7a-3p, let-7b-5p, and let-7b-3p did not change significantly (Fig. 4I–L).

3.6. TGFBR1 is the target of let-7a-5p

To discover the mechanisms underlying let-7a-5p-regulated anti-fibrotic effects, the target genes were predicted by using the online miRNA prediction websites (Targetminer, miRWalk, starBase, and mirDIP), and then we selected the genes overlapping those located in TGF-β signaling pathways predicted by KEGG using the DIANA tool. At last, TGFBR1, an important receptor of the TGF-β signaling pathway, was identified to be the target gene of let-7a-5p (Fig. 5A).

To make sure this prediction, the dual-luciferase reporter assay was used to clarify if let-7a-5p directly targets TGFBR1 in CDFs. The

predicted binding sites of let-7a-5p and TGFBR1 were shown (Fig. 5A). What we found was overexpression of let-7a-5p inhibited wildtype-let-7a-5p, instead of mutant reporter activity (Fig. 5B). qPCR results demonstrated that let-7a-5p mimics significantly up-regulated the level of let-7a-5p, while let-7a-5p inhibitor significantly down-regulated the level of let-7a-5p in CDFs (Fig. 5C). In line with this finding, both PCR and western blot results showed that let-7a-5p mimics significantly inhibited and let-7a-5p inhibitor significantly enhanced TGFBR1 expression (Fig. 5D–F).

3.7. The anti-fibrotic effect of BMSC-EVs depends on exosomal let-7a-5p

We tested the TGFBR1 and p-Smad2/3 expression on patient samples and found that both proteins were highly expressed in the SS group (Supplemental Fig. 12), which were involved in the TGF-β signaling pathway and considered as pathway markers for fibrosis in the following experiments. Afterward, we questioned whether the anti-fibrotic effect of BMSC-EVs was dependent on exosomal let-7a-5p. To verify the effects of let-7a-5p, we first treated BMSCs with the let-7a-5p inhibitor (50 nM) for 24 h before these cells were collected, and then fresh non-EVs DMEM was added for another 48 h (Fig. 6A). After that, the BMSCs and EVs were subjected to qPCR analysis. The results showed that let-7a-5p was significantly knocked down by its inhibitor in both BMSCs and EVs

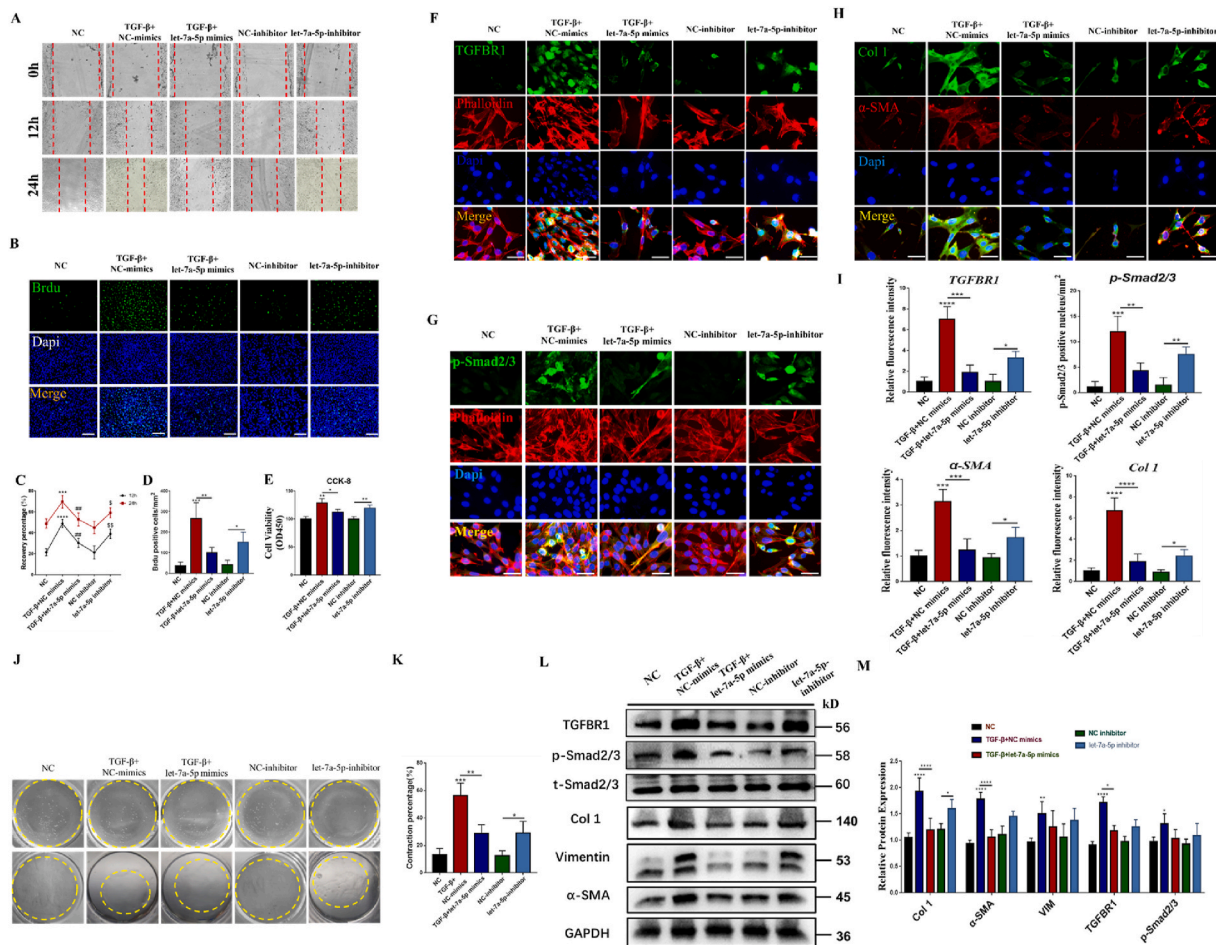


Fig. 8. Let-7a-5p inhibited CDF fibrogenesis induced by TGF- β *in vitro*. (A) The cell migration ability of CDFs was determined by wound-healing assay after different treatments. (B) Cell proliferation ability of CDFs was determined using BrdU incorporation assay after TGF- β stimulation with or without let-7a-5p mimics or let-7a-5p inhibitor treatment for 24h. Green signal = BrdU. Scale bar = 180 μ m. (C–D) Quantification of BrdU and wound-healing data (n = 3). Data are presented as mean \pm SD. *P < 0.05, **P < 0.01, ***P < 0.001, ****P < 0.0001, ###P < 0.01, # compared with TGF- β group, \$ P < 0.05, \$\$ P < 0.01, \$\$\$ compared with NC inhibitor group. (E) Cell proliferation ability of CDFs was further determined using CCK-8 assay. (n = 3) Data are presented as mean \pm SD. *P < 0.05, **P < 0.01. (F) Immunofluorescence was used to detect relative expression and distribution of TGFBR1 with different treatments. Scale bar = 50 μ m. (G) Immunofluorescence was used to detect relative expression and distribution of p-Smad2/3 with different treatments. Scale bar = 25 μ m. (H) Immunofluorescence was used to detect relative expression and distribution of collagen 1 and α -SMA with different treatments. Scale bar = 25 μ m. (I) Relative fluorescence intensity of TGFBR1, p-Smad2/3, collagen 1, and α -SMA after different treatments. (n = 3) Data are presented as mean \pm SD. **P < 0.01, ***P < 0.001, ****P < 0.0001. (J) The representative image of the ability of collagen contraction of CDFs in different groups (yellow dotted line indicated the collagen gel). (K) The contraction percentages of collagen gel in different groups compared to that of group NC at 24h. (n = 3) Data are presented as mean \pm SD. *P < 0.05, **P < 0.01, ***P < 0.001. (L–M) TGFBR1, p-Smad2/3, t-Smad2/3, VIMENTIN, and α -SMA protein levels in CDFs were determined by western blot after different treatments. (n = 4) Data are presented as mean \pm SD. *P < 0.05, ****P < 0.0001.

(BMSC-EVs^{let-7a-D}) (Fig. 6B–C). Based on the aforementioned data, BMSC-EVs inhibited TGF- β related fibrotic phenotypes. Thus, we administered BMSC-EVs or BMSC-EVs^{let-7a-D} into CDFs, and we found that let-7a-5p-knocked down significantly inhibited the anti-fibrotic effect of BMSC-EVs. In detail, CCK-8 cell viability, BrdU cell proliferation ability, and wound healing ability suppressed by BMSC-EVs were re-upregulated in the BMSC-EVs^{let-7a-D} group (Fig. 6D–H). Meanwhile, western blot and immunofluorescence results showed that the expression of TGFBR1, p-Smad2/3, Col 1, and α -SMA, which were suppressed by BMSC-EVs and re-elevated in the BMSC-EVs^{let-7a-D} group (Fig. 6I–L).

To make our findings more robust, NIH3T3 fibroblasts were applied to be co-incubated with TGF- β , BMSC-EVs, and BMSC-EVs^{let-7a-D}. BrdU staining, wound healing assay, and CCK-8 assay indicated the profibrotic activities and migration ability of NIH3T3 suppressed by BMSC-EVs, were reversed in the BMSC-EVs^{let-7a-D} group (Supplemental Figs. 13A–13E). Additionally, immunofluorescence showed BMSC-EVs-inhibited Col 1 and α -SMA expression were re-upregulated by let-7a-5p-knocked down (Supplemental Figs. 13F–13G).

Meanwhile, to further verify the above results, we injected a high concentration (50 μ l EV, 50ug/ml, 3×10^8) of BMSC-EVs or BMSC-EVs^{let-7a-D} in the SS model mice. Not surprisingly, we found that either ROM, capsular thickness, fibrotic marker expression, or cell infiltration relieved by BMSC-EVs treatment was reversed by let-7a-5p-knocked down (Fig. 7A–F).

3.8. Let-7a-5p mediate anti-fibrotic effect both *in vitro* and *in vivo*

Subsequently, a series of experiments were conducted to verify the anti-fibrotic potential of let-7a-5p. To avoid TGF-beta or EVs induced cell viability change, serum-free DMEM was used for cell intervention. For CDFs, let-7a-5p mimics significantly inhibited CCK-8 cell viability, BrdU cell proliferation ability, and wound healing ability induced by TGF- β , while let-7a-5p inhibitor enhanced BrdU staining, wound healing activity, and CCK-8 viability (Fig. 8A to E). Additionally, the high levels of TGFBR1, p-Smad2/3, Col 1, and α -SMA stimulated by TGF- β were significantly inhibited by let-7a-5p mimics presented by western blot

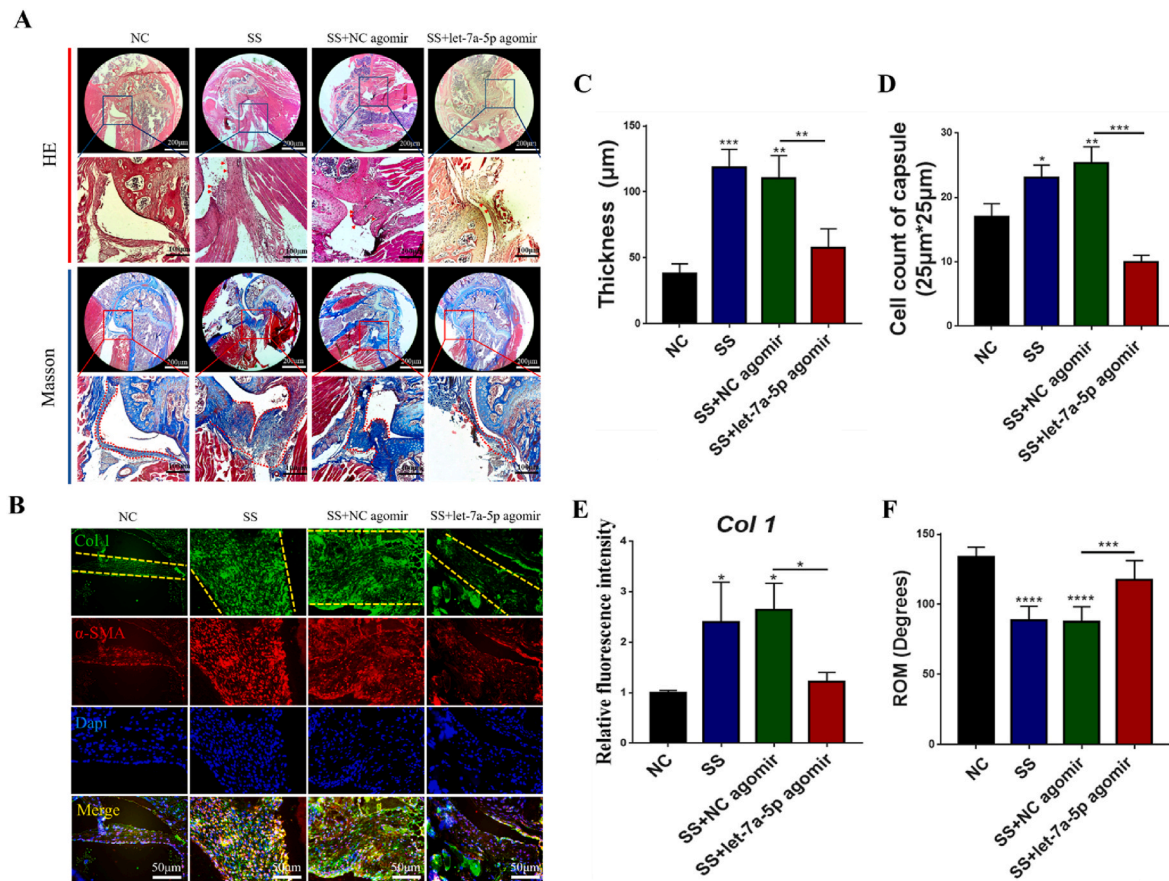


Fig. 9. The impact of let-7a-5p agomir on the histological and biomechanical appearance of mice shoulders with immobilization. (A) The representative image of the joint capsule of the shoulder on HE staining and Masson staining. Scale bar = 200 or 100 μm. The red arrow indicated the hypercellular status of the joint capsule. The red dotted line indicated the inner and outer border of the joint capsule. (B) Representative immunofluorescence images showed the location and relative expression of Collagen 1 and α-SMA in the mice capsular samples. Scale bar = 50 μm. (C) Quantification of capsule thickness and inter-group comparison. (n = 3) **P < 0.01. ***P < 0.001. (D) Cell number of shoulder capsule was counted. (n = 3) *P < 0.05, **P < 0.01, ***P < 0.001. (E) Relative fluorescence intensity of α-SMA with different treatments. (n = 3) *P < 0.05. (F) Quantification of passive range of motion. (n = 6) ***P < 0.001. ****P < 0.0001. Data are presented as mean ± SD.

and immunofluorescences, while the let-7a-5p inhibitor exerted the opposite effects that promoted those protein expressions (Immunofluorescences shown in Fig. 8E–G, quantified by 8I and western blot presented by 8L, quantified by 8M). Furthermore, the high contraction ability induced by TGF-β was suppressed by let-7a-5p mimics, in contrast, the let-7a-5p inhibitor showed the opposite effects that promoted the contraction ability of normal CDFs (Fig. 8J to K).

To make our findings more solid, we once again performed those experiments mentioned above on the NIH3T3 cell line. Similarly, For NIH3T3 cells, let-7a-5p mimics significantly inhibited CCK-8 cell viability, BrdU cell proliferation ability, and wound healing ability stimulated by TGF-β, while let-7a-5p inhibitor promoted BrdU staining, wound healing activity, and CCK-8 viability (Supplemental Figs. 14A–E). Additionally, the high levels of Col 1 and α-SMA stimulated by TGF-β were significantly inhibited by let-7a-5p mimics presented by immunofluorescences, while the let-7a-5p inhibitor exerted the opposite effects that promoted those protein expressions (Supplemental Figs. 14F–G).

For *in vivo* experiments, one single intra-articular injection of the agomir of let-7a-5p was administered to the index shoulder of the SS-model mouse at the start of the fourth week following immobilization three times. Then three weeks after the first injection, samples were harvested. HE staining results showed that prominent cell infiltration occurred in the shoulder capsule of three SS groups than in samples of the NC group (Fig. 9A and quantified in 9D). Besides, Masson staining suggested thickened capsules of four SS groups were exhibited than capsules of NC group. However, the thickness of the capsular SS +

agomir-let-7a-5p group was significantly lower than that of the SS group or SS + agomir-NC group (Fig. 9A and quantified in 9C). Moreover, for immunohistology, the expression of both Col 1 and α-SMA remarkably accumulated in the capsule of four SS groups than of the NC group, but this accumulation was remarkably lower in the SS + agomir-let-7a-5p group than that of the SS group or SS + agomir-NC group (Fig. 9B and quantified in 9E). Correspondingly, the ROM of the SS + agomir-let-7a-5p group was significantly higher than that of the SS group or the SS + agomir-NC group (Fig. 9F).

To verify the fibrotic role of TGFBR1, we knocked down the expression of TGFBR1 in CDFs by si-RNA. Western blot results indicated the efficiency of the TGFBR1 knock-down (Fig. 10A). BrdU assay and CCK-8 test found that suppressing the level of TGFBR1 inhibited the cell viability of CDFs (Fig. 10B–D). In addition, the high contraction ability induced by TGF-β was suppressed by TGFBR1 knockdown (Figs. 10I and 1J). Co-immunofluorescence staining showed that knock-down of TGFBR1 (Fig. 10E and H) inhibited the expression of α-SMA, Col 1, and p-Smad2/3 in CDFs challenged with TGF-β (Fig. 10F–H). The activities of TGF-β/Smad signaling were then observed. Western blot presented that TGF-β up-regulated, and siRNA down-regulated the level of TGFBR1 (Fig. 10K and quantified in 10L). Consistent with this trend, TGF-β ascended the level of downstream p-Smad2/3 level, Col 1, VIM, and α-SMA protein levels, which were all descended by siRNAs (Fig. 10K and L).

In sum, these observations implied that the anti-fibrotic effect of human BMSC-EVs was dependent on exosomal let-7a-5p targeting TGFBR1 (Fig. 11).

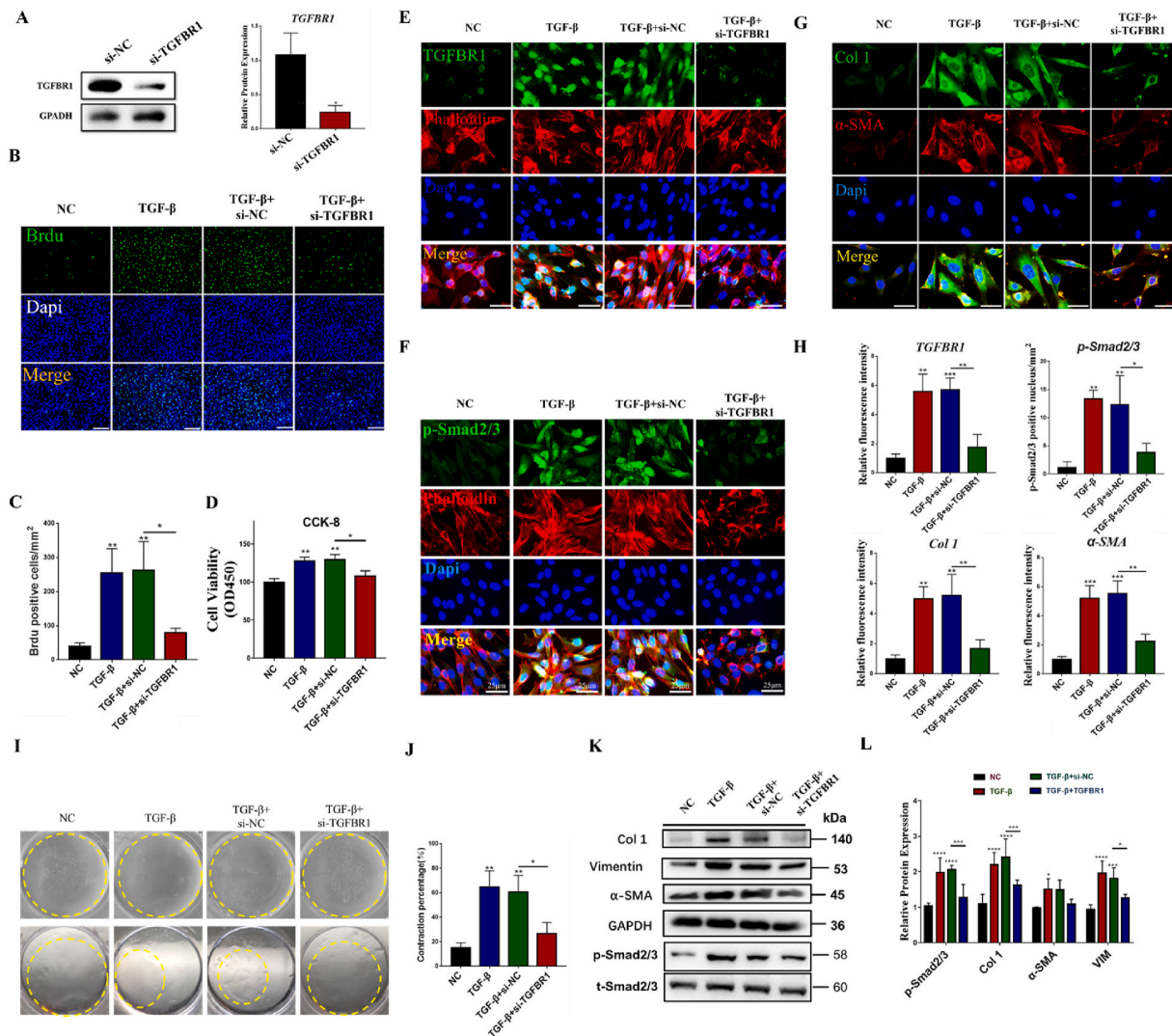


Fig. 10. TGFBR1 mediated TGF- β induced CDF fibrogenesis. (A) The expression level of TGFBR1 in CDF cells was determined 24h after si-TGFBR1 or si-NC. GAPDH was used as an internal control. (n = 3) Data are presented as mean \pm SD. *P < 0.05. (B) Cell proliferation ability of CDFs was determined using BrdU incorporation assay after different treatments. Green signal = BrdU. Scale bar = 180 μ m. (C) Quantification of BrdU data (n = 3). Data are presented as mean \pm SD. *P < 0.05, **P < 0.01. (D) Cell proliferation ability of CDFs was further determined using CCK-8 assay. (n = 3) Data are presented as mean \pm SD. *P < 0.05. ***P < 0.01. (E–G) Representative immunofluorescence images show the location and relative expression of TGFBR1, p-Smad2/3, Collagen 1, and α -SMA in the mice capsular samples. Scale bar = 50 or 25 μ m. (H) Relative fluorescence intensity of TGFBR1, p-Smad2/3, Col 1, and α -SMA with different treatments. (n = 3) Data are presented as mean \pm SD. *P < 0.05, **P < 0.01, ***P < 0.001. (I) The representative image of collagen contraction of CDFs in different groups (yellow dotted line indicated the collagen gel). (J) The contraction percentages of collagen gel in different groups compared to that of group NC at 24h. (n = 3) Data are presented as mean \pm SD. *P < 0.05, **P < 0.01. (K–L) The expression level of Col 1, Vimentin, α -SMA, p-Smad2/3, and t-Smad2/3 in CDF cells was determined 24h after different treatments by Western blotting. GAPDH was used as an internal control. (n = 3) Data are presented as mean \pm SD. *P < 0.05, ***P < 0.001, ****P < 0.0001.

4. Discussion

The current study demonstrated that BMSC-EVs could inhibit TGF- β induced fibroblast activation and collagen secretion *in vitro* and attenuate capsular stiffness in the mouse model *in vivo*. This therapeutic effect was related to exosomal let-7a-5p, a highly expressed miRNA in BMSC-EVs. By targeting TGFBR1, the miRNA blocked, at least partially, the TGF- β /Smad signaling pathway to inhibit fibrogenesis.

As aforementioned, driven by inflammation, a large number of fibroblasts are recruited in the shoulder capsule, and then secrete a large amount of collagen, leading to stiffness [10,12,13]. Therefore, promoting collagen degradation or inhibiting the secretion of collagen by fibroblasts has become the focus of anti-fibrosis for SS. Some animal studies have performed collagenase injection to treat SS, which resulted in good outcomes [51–53]. However, as collagen is an indispensable part of the extracellular matrix, it is not clear whether collagenase could

be utilized in clinical practice or not [54]. Alternatively, we proved the possibility of collagen secretion inhibition by BMSC-EVs, of which the effect relied on TGF- β /Smad signaling.

In the process of fibrosis, TGF- β signaling is typically activated. As for the canonical TGF- β signaling pathway, TGF- β molecules bind with membrane receptor TGFBR2 to activate TGFBR1. Next, Smad2 and Smad3 are recruited and activated by phosphorylation. Then, pSmad2/3 was transported into the nucleus with Smad4 to induce the synthesis of extracellular matrix [55,56]. TGF- β /Smad signaling is a positive feedback pathway, in which TGF- β can induce the expression of membrane receptors [56]. Thus, strategies to break this positive circle have been investigated to generate anti-fibrotic therapies [21,57]. For instance, miRNA let-7b represented a potential new target for the treatment of renal fibrosis in nephropathy by downregulating TGFBR1 [58], while long noncoding RNA-SNHG20 enhanced lung fibrosis via inhibiting miR-490 to up-regulate TGFBR1 [39]. Our findings also demonstrated

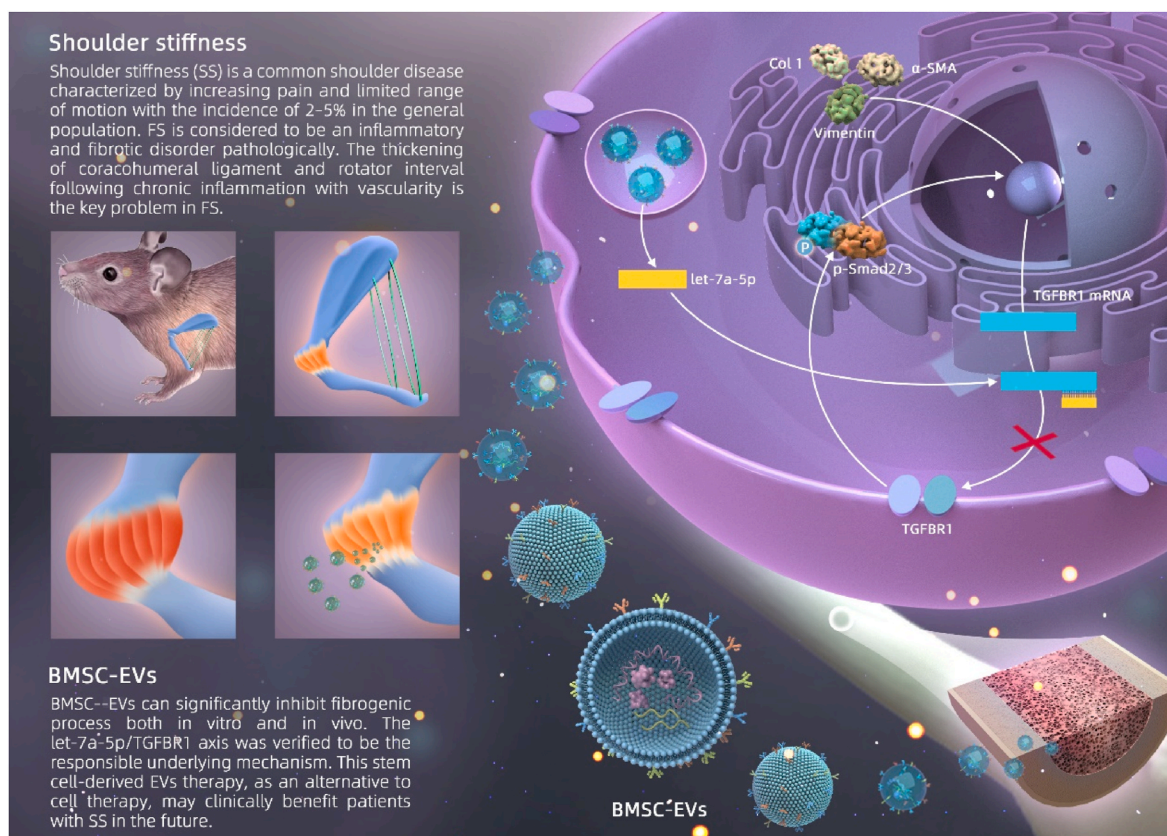


Fig. 11. Schematic depiction of this work. Human bone marrow mesenchymal stem cell-derived EVs inhibit capsular fibrosis via transferring let-7a-5p and targeting TGFBR1 mRNA.

that, for patients with shoulder stiffness, BMSC-EVs with their unique exosomal miRNAs constitution, targeted the TGFBR1 mRNA, confirming the pivotal role of this signaling pathway pathogenically and therapeutically.

CDFs have been a commonly applied model *in vitro* for investigating fibrosis-related mechanisms, especially FS, which are abundant in capsule tissue and retain the original features when passaged [41,59]. As for fibroblasts with pro-fibrotic phenotype, cell viability, proliferation rate, and migration ability are always up-regulated [60]. By using CCK-8, BrdU, and wound healing assay, the pro-fibrotic ability of fibroblasts was assessed. Besides, α -SMA, Col 1, and VIM have been widely accepted hallmarks of fibrosis, and are the direct fibrogenesis evidence [61]. In addition, the contraction ability was assessed by contraction test due to typically, the contraction ability of fibrosis is enhanced in activated fibroblasts [41]. A comprehensive evaluation of the status of fibroblasts in our study could be reached based on these biomarkers. In this study, BMSC-Exos and let-7a-5p significantly reduced TGF- β induced strong pro-fibrotic/collagen contraction ability and high-expressed fibrotic markers in a concentration-dependent manner. Those phenomena were similar to Fang's study that umbilical cord-derived exosomes inhibited myofibroblast activation and down-regulated α -SMA expression [62].

As for *in vivo* experiments, the shoulder immobilization model in rodents, given the similarity to what happened in patients with shoulder stiffness, e.g., infiltration of inflammatory cells, thickening of the joint capsule, and loss of ROM, is appropriate to study the pathology of FS [45,59,63]. In this study, by evaluating the expression of Col 1 and α -SMA, quantifying the thickness/cell number of the capsule, and measuring the ROM, we confirmed the anti-fibrotic effect of BMSC-Exos as well as let-7a-5p/TGFBR1 axis through forward and reversed argumentation (knockdown/agomir experiments).

Based on miRNAs sequencing and subsequent functional

verifications, it was exosomal let-7a-5p that exerted the anti-fibrotic role. This was also supported by various studies. For example, Matsuura et al. noticed that circulating let-7a-5p in serum may serve as a surrogate marker for the severity of hepatic fibrosis [64]. Wu et al. found that the remarkably decreased expression of let-7a accelerated liver fibrosis in their laboratory study [65]. Downregulation of let-7a was observed in scleroderma, resulting in the excessive deposition of collagen and tissue fibrosis of skin [66]. Papadopoulos et al. found that let-7a-5p could be a therapeutic target towards ureteropelvic junction obstruction through suppressing fibrosis [67].

Our findings could also lead to important potential implications that BMSC-EVs with their specific enriched miRNA might act as a potential strategy for the intercellular transfer of RNA molecules *in vivo*. Compared with other transfection strategies, we believe that the BMSC-EVs-based approach might be safer and more efficient since it naturally stimulates the endogenous mechanism for cell-cell communications [33, 68]. Compared with BMSC transplantation, many other advantages of BMSC-EVs in clinical applications can be easily expected, such as simpler production/storage procedures, easier quality control without the risk of tumorigenesis, and a lower risk of side effects [33,69–72]. Therefore, we believe that BMSC-EVs-based therapy could be a candidate strategy for clinical SS treatment in the future.

There are several limitations in the current study that should be noted. First, we just utilized the adult mice model to study the effects of BMSC-EVs on capsular fibrosis. However, SS is complex in pathogenesis and multi-factor in clinical practice [73]. Further study should consider verifying the therapeutic effects of BMSC-EVs in other animal models. Second, shoulder immobilization is only performed on young healthy animals. The effects of BMSC-EVs may differ in senescent cells with altered genetic or epigenetic content in old patients. Third, the potential xenogeneic response may arise that we utilized human-derived EVs to treat murine cell line, though some studies had already utilized human

BMSC-EVs to co-culture with murine cell lines, such as murine 5T33MM model [74], murine Lewis lung carcinoma cell line [75], and murine dorsal root ganglia [76].

5. Conclusion

In summary, our study elucidated the antifibrotic role of BMSC-EVs in capsular fibrosis, which was achieved by transferring let-7a-5p and suppressing TGFBR1 expression. This study clarifies a new approach using stem cell-derived EVs therapy as an alternative to cell therapy, which may clinically benefit patients with frozen shoulder in the future.

Funds

Supported by the project of the National Natural Science Foundation of China (grant number 82102634; 82172509; 81772419; 81972062) and original scientific personalized supporting project of Huashan Hospital (Fudan University, 2020).

Data availability statement

The datasets used and/or analyzed during the current study are available from the corresponding author on reasonable request.

CRediT authorship contribution statement

Zhiwen Luo: Investigation, Methodology, Formal analysis, Writing – review & editing. **Yaying Sun:** Methodology, Formal analysis, Investigation. **Beijie Qi:** Formal analysis, Investigation. **Jinrong Lin:** Formal analysis, Investigation. **Yisheng Chen:** Methodology, Investigation. **Yuzhen Xu:** Investigation. **Jiwu Chen:** Conceptualization, Visualization, Writing – review & editing.

Declaration of competing interest

The authors declare that they have no competing interests, and all authors should confirm its accuracy.

Acknowledgments

The authors thank all of the members of the laboratory of Shanghai Institute of Nutrition and Health (CAS) for their encouragement and assistance in this study. Sequencing service were provided by Personal Biotechnology Co., Ltd. Shanghai, China.

Appendix A. Supplementary data

Supplementary data to this article can be found online at <https://doi.org/10.1016/j.bioactmat.2022.01.016>.

References

- [1] Y. Sun, et al., Intra-articular steroid injection for frozen shoulder: a systematic review and meta-analysis of randomized controlled trials with trial sequential analysis, *Am. J. Sports Med.* 45 (2017) 2171–2179.
- [2] Y. Sun, S. Lu, P. Zhang, Z. Wang, J. Chen, Steroid injection versus physiotherapy for patients with adhesive capsulitis of the shoulder, *Medicine (Baltimore)*. 95 (2016) e3469.
- [3] M. Pietrzak, Adhesive capsulitis: an age related symptom of metabolic syndrome and chronic low-grade inflammation? *Med. Hypotheses* 88 (2016) 12–17.
- [4] Y. Sun, S. Liu, S. Chen, J. Chen, The effect of corticosteroid injection into rotator interval for early frozen shoulder: a randomized controlled trial, *Am. J. Sports Med.* 46 (2018) 663–670.
- [5] D.A.W.M. Van Der Windt, B.W. Koes, B.A. De Jong, L.M. Bouter, Shoulder disorders in general practice: incidence, patient characteristics, and management, *Ann. Rheum. Dis.* (1995), <https://doi.org/10.1136/ard.54.12.959>.
- [6] M. Lubiecki, A. Carr, Frozen shoulder: past, present, and future, *J. Orthop. Surg.* 15 (2007) 1–3.
- [7] J.E. Hsu, O.A. Anakwenze, W.J. Warrender, J.A. Abboud, Current review of adhesive capsulitis, *J. Shoulder Elbow Surg.* 20 (2011) 502–514.
- [8] Y. Sun, J. Lin, Z. Luo, J. Chen, Preoperative lymphocyte to monocyte ratio can be a prognostic factor in arthroscopic repair of small to large rotator cuff tears, *Am. J. Sports Med.* 48 (2020) 3042–3050.
- [9] G. Harris, P. Bou-Haidar, C. Harris, Adhesive capsulitis: review of imaging and treatment, *J. Med. Imaging Radiat. Oncol.* 57 (2013) 633–643.
- [10] J.D. Zuckerman, A. Rokito, Frozen shoulder: a consensus definition, *J. Shoulder Elbow Surg.* 20 (2011) 322–325.
- [11] M.F. Xue, et al., The treatment of fibrosis of joint synovium and frozen shoulder by Smad4 gene silencing in rats, *Med. Hypotheses* 11 (2005) 1–15.
- [12] J. Chen, et al., Pathological changes of frozen shoulder in rat model and the therapeutic effect of PPAR- γ agonist, *J. Orthop. Res.* 39 (2021). John Wiley & Sons, Ltd.
- [13] M.F. Xue, S.L. Gong, J.P. Dai, G. Chen, J.Y. Hu, The treatment of fibrosis of joint synovium and frozen shoulder by Smad4 gene silencing in rats, *PLoS One* 11 (2016) 1–15.
- [14] Y. Sun, S. Liu, S. Chen, J. Chen, The effect of corticosteroid injection into rotator interval for early frozen shoulder: a randomized controlled trial, *Am. J. Sports Med.* 46 (2018) 663–670.
- [15] Y. Sun, et al., Intra-articular steroid injection for frozen shoulder: a systematic review and meta-analysis of randomized controlled trials with trial sequential analysis, *Am. J. Sports Med.* 45 (2017) 2171–2179.
- [16] K. Takase, Oral steroid therapy for frozen shoulder, *W. Indian Med. J.* 59 (2010) 674–679.
- [17] K.H. Kim, J.W. Suh, K.Y. Oh, The effect of intra-articular hyaluronate and tramadol injection on patients with adhesive capsulitis of the shoulder, *J. Back Musculoskelet. Rehabil.* 30 (2017) 913–920.
- [18] E. Itoi, et al., Shoulder stiffness: current concepts and concerns, *Arthrosc. J. Arthrosc. Relat. Surg. Off. Publ. Arthrosc. Assoc. North Am. Int. Arthrosc. Assoc.* 32 (2016) 1402–1414.
- [19] D.C. Rockey, P.D. Bell, J.A. Hill, Fibrosis — a common pathway to organ injury and failure, *N. Engl. J. Med.* 372 (2015) 1138–1149.
- [20] Z. Luo, J. Lin, Y. Sun, C. Wang, J. Chen, Bone marrow stromal cell-derived exosomes promote muscle healing following contusion through macrophage polarization, *Stem Cell. Dev.* 30 (2021) 135–148.
- [21] N.C. Henderson, F. Rieder, T.A. Wynn, Fibrosis: from mechanisms to medicines, *Nature* 587 (2020) 555–566.
- [22] D.M. Pegtel, S.J. Gould, Exosomes. *Annu. Rev. Biochem.* 88 (2019) 487–514.
- [23] H.A. Çakmak, M. Demir, MicroRNA and cardiovascular diseases, *Balkan Med. J.* (2020), <https://doi.org/10.4274/balkanmedj.galenos.2020.2020.1.94>.
- [24] X. Santamaria, H. Taylor, MicroRNA and gynecological reproductive diseases, *Fertil. Steril.* (2014), <https://doi.org/10.1016/j.fertnstert.2014.04.044>.
- [25] T.G. Ruksha, A.V. Komina, N.V. Palkina, MicroRNA in skin diseases, *Eur. J. Dermatol.* 27 (2017) 343–352.
- [26] H. Wang, et al., Exosome-mediated miR-29 transfer reduces muscle atrophy and kidney fibrosis in mice, *Mol. Ther.* 27 (2019) 571–583.
- [27] Y. Shi, et al., Immunoregulatory mechanisms of mesenchymal stem and stromal cells in inflammatory diseases, *Nat. Rev. Nephrol.* 14 (2018) 493–507.
- [28] G.R. Willis, et al., Mesenchymal stromal cell exosomes ameliorate experimental bronchopulmonary dysplasia and restore lung function through macrophage immunomodulation, *Am. J. Respir. Crit. Care Med.* 197 (2018) 104–116.
- [29] J.Y. Cao, et al., Exosomal miR-125b-5p deriving from mesenchymal stem cells promotes tubular repair by suppression of p53 in ischemic acute kidney injury, *Theranostics* 11 (2021) 5248–5266.
- [30] J.M. Aliotta, et al., Exosomes induce and reverse monocrotaline-induced pulmonary hypertension in mice, *Cardiovasc. Res.* 110 (2016) 319–330.
- [31] W. Zhu, et al., Macrophage migration inhibitory factor facilitates the therapeutic efficacy of mesenchymal stem cells derived exosomes in acute myocardial infarction through upregulating miR-133a-3p, *J. Nanobiotechnol.* 19 (2021) 1–16.
- [32] Z. Wang, Y. Wu, Z. Zhao, C. Liu, L. Zhang, Study on transorgan regulation of intervertebral disc and extra-skeletal organs through exosomes derived from bone marrow mesenchymal stem cells, *Front. Cell Dev. Biol.* 9 (2021) 1–11.
- [33] Y. Wang, et al., Exosomes derived from miR-214-enriched bone marrow-derived mesenchymal stem cells regulate oxidative damage in cardiac stem cells by targeting CaMKII, *Oxid. Med. Cell. Longev.* (2018), 4971261, 2018.
- [34] V. Sengupta, et al., Exosomes derived from bone marrow mesenchymal stem cells as treatment for severe COVID-19, *Stem Cell. Dev.* 29 (2020) 747–754.
- [35] S. Gurung, S. Williams, J.A. Deane, J.A. Werkmeister, C.E. Gargett, The transcriptome of human endometrial mesenchymal stem cells under TGF β R inhibition reveals improved potential for cell-based therapies, *Front. Cell Dev. Biol.* 6 (2018) 1–15.
- [36] H. Fazaeli, et al., A comparative study on the effect of exosomes secreted by mesenchymal stem cells derived from adipose and bone marrow tissues in the treatment of osteoarthritis-induced mouse model, *BioMed Res. Int.* 2021 (2021).
- [37] M. Pomatto, et al., Differential therapeutic effect of extracellular vesicles derived by bone marrow and adipose mesenchymal stem cells on wound healing of diabetic ulcers and correlation to their cargoes, *Int. J. Mol. Sci.* 22 (2021) 1–26.
- [38] F. Gao, et al., Protective function of exosomes from adipose tissue-derived mesenchymal stem cells in acute kidney injury through SIRT1 pathway, *Life Sci.* 255 (2020), 117719.
- [39] D. Cheng, et al., Long noncoding RNA-SNHG20 promotes silica-induced pulmonary fibrosis by miR-490-3p/TGFBR1 axis, *Toxicology* 451 (2021), 152683.
- [40] J. Chen, S. Chen, Y. Li, Y. Hua, H. Li, Is the extended release of the inferior glenohumeral ligament necessary for frozen shoulder? *Arthrosc. J. Arthrosc. Relat. Surg.* 26 (2010) 529–535.
- [41] Y. Sun, J. Lin, Z. Luo, Y. Zhang, J. Chen, The serum from patients with secondary frozen shoulder following rotator cuff repair induces shoulder capsule fibrosis and

- promotes macrophage polarization and fibroblast activation, *J. Inflamm. Res.* 14 (2021) 1055–1068.
- [42] J. Zhang, J. Wu, The potential roles of exosomal miR-214 in bone metastasis of lung adenocarcinoma, *Front. Oncol.* 10 (2021).
- [43] C. Théry, et al., Minimal information for studies of extracellular vesicles 2018 (MISEV2018): a position statement of the International Society for Extracellular Vesicles and update of the MISEV2014 guidelines, *J. Extracell. Vesicles* 7 (2018), 1535750.
- [44] K. Chen, T. Yu, X. Wang, Inhibition of circulating exosomal miRNA-20b-5p accelerates diabetic wound repair, *Int. J. Nanomed.* 16 (2021) 371–381.
- [45] J.C. Villa-Camacho, et al., In vivo kinetic evaluation of an adhesive capsulitis model in rats, *J. Shoulder Elbow Surg.* 24 (2015) 1809–1816.
- [46] A. Kanno, H. Sano, E. Itoi, Development of a shoulder contracture model in rats, *J. Shoulder Elbow Surg.* (2010), <https://doi.org/10.1016/j.jse.2010.02.004>.
- [47] S. Oki, et al., Generation and characterization of a novel shoulder contracture mouse model, *J. Orthop. Res. Off. Publ. Orthop. Res. Soc.* 33 (2015) 1732–1738.
- [48] Z.W. Luo, et al., Establishment of an adult zebrafish model of retinal neurodegeneration induced by NMDA, *Int. J. Ophthalmol.* 12 (2019) 1250–1261.
- [49] Y. Sun, et al., A synthetic bridging patch of modified co-electrospun dual nano-scaffolds for massive rotator cuff tear, *J. Mater. Chem. B* 4 (2016) 7259–7269.
- [50] W. Chen, et al., Conditioned medium of human bone marrow-derived stem cells promotes tendon-bone healing of the rotator cuff in a rat model, *Biomaterials* 271 (2021), 120714.
- [51] C.H. Cho, Y.M. Lho, I. Hwang, D.H. Kim, Role of matrix metalloproteinases 2 and 9 in the development of frozen shoulder: human data and experimental analysis in a rat contracture model, *J. Shoulder Elbow Surg.* 28 (2019) 1265–1272.
- [52] A.M.T. Lubis, V.K. Lubis, Matrix metalloproteinase, tissue inhibitor of metalloproteinase and transforming growth factor-beta 1 in frozen shoulder, and their changes as response to intensive stretching and supervised neglect exercise, *J. Orthop. Sci.* 18 (2013) 519–527.
- [53] N. Karahan, et al., Can collagenase Be used in the treatment of adhesive capsulitis? *Med. Princ. Pract.* 29 (2020) 174–180.
- [54] J. Fitzpatrick, C. Richardson, I. Klaber, M.D. Richardson, Clostridium histolyticum (Aa4500) for the treatment of adhesive capsulitis of the shoulder: a randomised double-blind, placebo-controlled study for the safety and efficacy of collagenase – single site report, *Drug Des. Dev. Ther.* 14 (2020) 2707–2713.
- [55] L. Wang, H.L. Wang, T.T. Liu, H.Y. Lan, TGF-beta as a master regulator of diabetic nephropathy, *Int. J. Mol. Sci.* 22 (2021) 1–18.
- [56] X.M. Meng, D.J. Nikolic-Paterson, H.Y. Lan, TGF- β : the master regulator of fibrosis, *Nat. Rev. Nephrol.* 12 (2016) 325–338.
- [57] X. Zhao, J.Y.Y. Kwan, K. Yip, P.P. Liu, F.F. Liu, Targeting metabolic dysregulation for fibrosis therapy, *Nat. Rev. Drug Discov.* 19 (2020) 57–75.
- [58] B. Wang, et al., Transforming growth factor- β 1-mediated renal fibrosis is dependent on the regulation of transforming growth factor receptor 1 expression by let-7b, *Kidney Int.* 85 (2014) 352–361.
- [59] M. Akbar, et al., Fibroblast activation and inflammation in frozen shoulder, *PLoS One* 14 (2019) 1–16.
- [60] Y. Sun, et al., miR-146a-5p acts as a negative regulator of TGF- β signaling in skeletal muscle after acute contusion, *Acta Biochim. Biophys. Sin.* 49 (2017) 628–634.
- [61] Y. Sun, et al., miR-24 and miR-122 negatively regulate the transforming growth factor- β /smad signaling pathway in skeletal muscle fibrosis, *Mol. Ther. Nucleic Acids* 11 (2018) 528–537.
- [62] S. Fang, et al., Umbilical cord-derived mesenchymal stem cell-derived exosomal microRNAs suppress myofibroblast differentiation by inhibiting the transforming growth factor- β /SMAD2 pathway during wound healing, *Stem Cells Transl. Med.* (2016).
- [63] R.S. Page, et al., Adhesive capsulitis of the shoulder: protocol for the adhesive capsulitis biomarker (AdCaB) study, *BMC Musculoskel. Disord.* 20 (2019) 4–9.
- [64] M. Matsuura, et al., A polydiagnostic and dimensional comparison of epileptic psychoses and schizophrenia spectrum disorders, *Schizophr. Res.* 69 (2004) 189–201.
- [65] N. Wu, et al., The secretin/secretin receptor axis modulates liver fibrosis through changes in transforming growth factor- β 1 biliary secretion in mice, *Hepatology* 64 (2016) 865–879.
- [66] K. Makino, et al., The downregulation of microRNA let-7a contributes to the excessive expression of type I collagen in systemic and localized scleroderma, *J. Immunol.* 190 (2013) 3905–3915.
- [67] T. Papadopoulos, et al., Systems biology combining human- and animal-data miRNA and mRNA data identifies new targets in ureteropelvic junction obstruction, *BMC Syst. Biol.* 11 (2017) 1–11.
- [68] D. Wu, et al., Exosomes derived from bone mesenchymal stem cells with the stimulation of Fe₃O₄ nanoparticles and static magnetic field enhance wound healing through upregulated miR-21-5p, *Int. J. Nanomed.* 15 (2020) 7979–7993.
- [69] X. Liu, et al., BMSC transplantation aggravates inflammation, oxidative stress, and fibrosis and impairs skeletal muscle regeneration, *Front. Physiol.* 10 (2019).
- [70] Y. Zhu, Y. Jia, Y. Wang, J. Xu, Y. Chai, Impaired bone regenerative effect of exosomes derived from bone marrow mesenchymal stem cells in type 1 diabetes, *Stem Cells Transl. Med.* 8 (2019) 593–605.
- [71] Y. Chen, K. Xue, X. Zhang, Z. Zheng, K. Liu, Exosomes derived from mature chondrocytes facilitate subcutaneous stable ectopic chondrogenesis of cartilage progenitor cells, *Stem Cell Res. Ther.* 9 (2018) 318.
- [72] C. Wang, Q. Hu, W. Song, W. Yu, Y. He, Adipose stem cell-derived exosomes decrease fatty infiltration and enhance rotator cuff healing in a rabbit model of chronic tears, *Am. J. Sports Med.* 48 (2020) 1456–1464.
- [73] W. Konarski, T. Poboży, M. Hordowicz, K. Poboży, J. Domańska, Current concepts of natural course and in management of frozen shoulder: a clinical overview, *Orthop. Rev.* 12 (2021).
- [74] J. Wang, et al., Bone marrow stromal cell-derived exosomes as communicators in drug resistance in multiple myeloma cells, *Blood* 124 (2014) 555–566.
- [75] X. Zhang, et al., Hypoxic BMSC-derived exosomal miRNAs promote metastasis of lung cancer cells via STAT3-induced EMT, *Mol. Cancer* 18 (2019) 40.
- [76] M.A. Lopez-Verrilli, et al., Mesenchymal stem cell-derived exosomes from different sources selectively promote neuritic outgrowth, *Neuroscience* 320 (2016) 129–139.